Orientation-dependence of Dislocation-induced Incipient Plasticity in Mg Via Nanoindentation Technique

By

Moein Imani Foumani

A Thesis Submitted to the Faculty of Graduate Studies of

The University of Manitoba

In partial fulfilment of the requirements of the degree of

MASTER OF SCIENCE

Department of Mechanical Engineering

University of Manitoba

Winnipeg, Manitoba

ABSTRACT

Magnesium (Mg) and its alloys have gained significant attention in recent years due to their lightweight nature and potential applications in transportation, aerospace, and biomedical industries. However, one of the major limitations to their broader application is the pronounced poor ductility. To better understand the root causes of this limitation, it is essential to investigate the plasticity across different crystallographic orientations.

This thesis investigates the onset of plastic deformation, with a particular focus on dislocation-mediated incipient plasticity in a coarse-grained Mg–2 wt.% Gd alloy using the nanoindentation technique. A nanoindentation protocol was designed to suppress the formation of deformation twins by applying low indentation loads (1000 μN), enabling the isolation and examination of dislocation nucleation events. A novel "grain signing–finding approach" was developed to accurately identify and repeatedly test specific grain orientations. This allowed for over 100 indents per orientation across 13 distinct grains, including basal, prismatic, and pyramidal orientations.

High-resolution scanning electron microscopy (HRSEM) and scanning probe microscopy (SPM) revealed no evidence of twinning, supporting that deformation at the nano-scale was mediated exclusively by dislocations. Load-displacement curves showed three distinct modes of the first pop-in event—(i) ideal pop-in, (ii) deviation before pop-in, and (iii) excursion before pop-in—all of which demonstrated strong orientation dependence. Furthermore, two types of pop-in sequences were observed: single and successive pop-ins, with successive events occurring only in basal orientations. The basal grains exhibited a higher median resolved shear stress (~1.3 GPa) compared to prismatic and pyramidal grains (~1.0 GPa), consistent with theoretical predictions for dislocation nucleation. This suggests the involvement of pyramidal ⟨c+a⟩ dislocations in basal orientations, facilitating plastic deformation along the c-axis. The activation volume associated with the first pop-in ranged from 27 to 40 $Å^3$—involving about ~2 atoms of magnesium—supporting a surface dislocation nucleation mechanism and ruling out twinning, which typically requires a much larger activation volume.

Interestingly, the observation of successive pop-ins in basal orientations, along with higher stress levels, suggests the possibility of a cross-slip nucleation mechanism to accommodate ⟨c⟩-axis deformation.

ACKNOWLEDGMENTS

I would like to express my gratitude to my supervisor, Dr. Guo-zhen Zhu, for her guidance and supervision throughout the completion of this work. I am also thankful to Yushun Liu and Syed Taha Khursheed for their insightful discussions, which significantly enhanced the quality of this research.

A heartfelt thank you goes to my friend and team member, Zhina Razaghi, for her support in both scientific collaboration and various leadership activities. I wish her continued success in her research endeavours. I am grateful to Farhang Parsa and Jian Yiu for their constructive feedback during group meetings, which helped improve the direction and depth of my research.

I would also like to extend my appreciation to Olanrewaju (Lanre) Ojo and Dr. Chuang Deng for serving on my thesis committee. Their thoughtful questions and valuable suggestions played a key role in shaping the clarity and focus of this study. Additionally, I would like to express my heartfelt thanks to Julia Osso Margolis for her invaluable support in helping me understand various aspects of student rights throughout my academic journey.

Finally, I am deeply thankful to my family and friends for their constant encouragement and support throughout this journey.

Table of Contents

LIST OF FIGURES

LIST OF TABLES

LIST OF COPYRIGHTED MATERIALS

1- Figure 2.1. a) Schematic of the Load-displacement curve after nanoindentation including the load, unload, elastic and plastic segments
Source: Nanoindentation. Mechanical Engineering Series
Author: Anthony C. Fischer-Cripps
Publisher: Springer
Copyright Number:1616515-1.

2- Figure 2.3. a) P–h curve showing small excursion (m) and pop-in (M); b) MD simulation of a 12 nm spherical indenter on Al <111> surface showing sessile structure from glide loops on {111} planes
Source: Atomistic mechanisms governing elastic limit and incipient plasticity in crystals
Author: Ju Li, Krystyn J Van Vliet, Ting Zhu, Sidney Yip, Subra Suresh
Publication: Acta Materialia
Publisher: Nature
License Number: 6040911040699

3- Figure 2.4. Formation of Lomer–Cottrell locks in pure Cu (111) orientation, showing the transition from half-PDLs to fully closed PDLs during successive pop-ins from a) to d) [86].
Source: Dislocation structure and dynamics govern pop-in modes of nanoindentation on single-crystal metals
Author: Nian Zhou, Khalil I. Elkhodary, Xiaoxu Huang, Shan Tang & Ying Li
Publication: Acta Materialia
Publisher: Taylor & Francis - Philosophical Magazine
License Number: tphm/05217015

4- Figure 2.7. Nanoindentation behaviors on pure Mg in different crystallographic orientations, a) P-h curves, b) corresponding AFM images of indenter impressions
Source: Twinning during nanoindentation of magnesium single crystals
Author: Jun Chung
Publisher: Deakin University
License Number: Under request

5- Figures 2.5. Atomic configurations of incipient plasticity during indentation in different steps in basal orientation [15].
Source: Effect of crystal orientation on incipient plasticity during nanoindentation of magnesium
Author: Hidetoshi Somekawa,Tomohito Tsuru,Alok Singh,Seiji Miura,Christopher A. Schuh
Publication: Acta Materialia
Publisher: Elsevier
License Number: 6040921149009

6- Figures 2.6. Atomic configurations of incipient plasticity during indentation in different steps in prismatic orientation [15].
Source: Effect of crystal orientation on incipient plasticity during nanoindentation of magnesium
Author: Hidetoshi Somekawa,Tomohito Tsuru,Alok Singh,Seiji Miura,Christopher A. Schuh
Publication: Acta Materialia
Publisher: Elsevier
License Number: 6040921149009

LIST OF SYMBOLS

E	Young's modulus
ν	Poisson's ratio
R	Radius of indenter (spherical tip)
P	Applied load
h	Indentation depth
a	Contact radius
σ	Stress
τ	Shear stress
V	Activation volume
k	Boltzmann constant
T	Temperature
m	Schmid factor
ρ	Dislocation density
h_c	Contact depth
A	Contact area
H	Hardness
S	Contact stiffness
t	Time
$\dot{\epsilon}$	Strain rate
μ	Shear modulus
γ	Shear strain
F	Force
b	Burgers vector
c/a	Lattice parameter ratio for HCP structures

LIST OF ABBREVIATION

Mg	Magnesium
Gd	Gadolinium
HCP	Hexagonal Close-Packed
CRSS	Critical Resolved Shear Stress
HRSEM	High-Resolution Scanning Electron Microscopy
SPM	Scanning Probe Microscopy
AFM	Atomic Force Microscopy
MD	Molecular Dynamics
EAM	Embedded Atom Method
EBSD	Electron Backscatter Diffraction
ISF	Indentation Schmid Factor
RSS	Resolved Shear Stress
P-h	Load–Displacement Curve
CPFEM	Crystal Plasticity Finite Element Method
CI	Confidence Index
SEM	Scanning Electron Microscopy
PDL	Prismatic Dislocation Loop
SR	Scan Rate
SP	Step Point
IG	Integral Gain
TV	Tip Velocity
SS	Scan Size

μN	Micronewton
μm	Micrometer
r.p.m.	Rotation per Minute
IPF	Inverse Pole Figure
OIM	Orientation Imaging Microscopy
3D-EBSD	3D Electron Backscatter Diffraction
TEM	Transmission Electron Microscopy
HEAs	High Entropy Alloys

Chapter 1- Introduction

1.1. Research Background

Magnesium (Mg) and its alloys stand among the most significant structural metals in contemporary engineering and manufacturing. Their importance is primarily due to a unique combination of properties, most notably their low density (1.74 g/cm³), especially when compared to other common structural metals such as iron (7.9 g/cm³), aluminium (2.7 g/cm³), and titanium (4.5 g/cm³) [1, 2] . This low density translates into substantial weight and cost savings in industries where lightweight materials are essential, including aerospace and transportation. From an environmental perspective, the resultant reduction in fuel consumption through lightweight design is highly beneficial in mitigating global warming concerns [3, 4]. Magnesium's relatively low melting temperature (approximately 650 °C), good castability, and weldability further enhance its industrial appeal by simplifying manufacturing processes and reducing overall production costs [5, 6]. As a result, Mg alloys have experienced a growing demand across various sectors, such as automotive, aerospace, electronics, biomedical, and energy systems [3]. Despite these benefits, magnesium alloys exhibit anisotropic mechanical behaviour, which is closely linked to the hexagonal close-packed (HCP) crystal structure of Mg [7-9]. In HCP systems, the critical resolved shear stress (CRSS) for basal ⟨a⟩ slip is significantly lower than for ⟨c⟩-component slips, such as pyramidal ⟨c+a⟩ and prismatic ⟨c⟩ slip. This CRSS disparity leads to limited deformation along the

⟨c⟩-axis, thus encouraging deformation twinning as a compensatory mechanism [1]. Consequently, the mechanical response of Mg is strongly orientation-dependent, frequently resulting in notable yield asymmetries in tension–compression tests [7, 9, 10].

To develop high-performance Mg alloys with reduced mechanical anisotropic properties, it is critical to understand the earliest stage of plastic deformation, known as “incipient plasticity” in various crystallographic orientations. This can help to understand the dominant deformation modes in different grain orientations.

Conventional macroscopic tests—such as tensile, compression, and hardness testing—cannot adequately capture the complex details of incipient plasticity because they probe a relatively large volume of material and combine multiple competing deformation mechanisms. In contrast, nanoindentation, with its ability to control minute loads and displacements over very small material volumes, offers a powerful tool for probing the onset of plastic deformation at the nanoscale.

Although nanoindentation studies have provided valuable insights into the incipient plasticity of Mg and its alloys, most investigations have focused on only a few low-index crystal orientations [11-15]. This narrow scope hinders our comprehensive understanding of orientation-dependent incipient plasticity. A major challenge is preparing single crystals or well-oriented grains across a wide spectrum of orientations, an endeavor often costly and time-consuming.

Another major challenge is the complexity of magnesium’s deformation mechanisms, which involve various types of dislocations and twinning. It is essential to decouple the inferences and contributions of each mechanism, as it can reveal more detailed insights into the fundamental processes governing incipient plasticity in each orientation.

1.2. Research Motivation

Magnesium’s anisotropic mechanical behaviour significantly limits its use across various industries. Mitigating this mechanical anisotropy requires a clear understanding of the dominant deformation modes in different crystallographic orientations. Using conventional mechanical testing methods, such as tensile, compression, or microhardness tests, is useful for bulk assessments, they typically involve multiple grain orientations at once. However, to develop new alloys with reduced anisotropy, it is crucial to first understand how incipient plasticity initiates in individual crystallographic orientations. As a result, these macroscale techniques have very limited capability to reveal how plastic deformation initiates or how it depends on crystallographic orientation. In this context, nanoscale mechanical testing techniques, particularly nanoindentation, enable localized probing of incipient plasticity within individual grains, thus shedding light on orientation-specific deformation mechanisms. Nanoindentation can also be strategically applied to isolate dislocation-mediated plasticity from twinning, thereby clarifying how dislocation activity alone evolves with orientation.

Despite substantial research efforts, most studies have concentrated on basal and prismatic orientations, leaving a gap in our understanding of how other crystallographic directions affect incipient plasticity. Furthermore, precisely disentangling dislocation-driven processes from twinning remains a significant challenge, yet is crucial for a thorough evaluation of dislocation-mediated incipient plasticity. Addressing these gaps will not only advance our fundamental understanding of orientation-dependent dislocation nucleation and behavior in Mg but also guide the development of high-performance Mg alloys with more predictable, and potentially more isotropic, mechanical properties.

1.3. Research Objectives and Thesis Structure

The primary goal of this thesis is to clarify the orientation dependence of incipient plasticity in magnesium, with a particular emphasis on dislocation-driven mechanisms. To achieve this goal, two main objectives have been defined:

1. Optimisation and development of nanoindentation for different crystallographic grains: In this objective, we optimised the nanoindentation methodology to specifically examine incipient plasticity with detectable pop-in. Additionally, we introduce a novel grain identification "signing-finding approach", enabling systematic investigation across a wide range of crystallographic orientations.

2. Study orientation-dependent incipient plasticity: Investigate how varying crystal orientations influence the critical stress, pop-in behavior, activation volume, and underlying dislocation mechanisms governing incipient plasticity.

The thesis is organized into five chapters:

- **Chapter 1** introduces the research background, highlights the motivation, and outlines the primary objectives and structure of the study.

- **Chapter 2** provides a comprehensive literature review, covering the fundamentals of nanoindentation, existing findings on incipient plasticity across different alloys, and emphasising the key challenges and knowledge gaps specific to magnesium.
- **Chapter 3** details the experimental methodology, including sample preparation, orientation characterization, and the design of nanoindentation tests tailored to capture dislocation-dominated behavior.
- **Chapter 4** presents and discusses the experimental results, focusing on pop-in events, stress calculations, activation volumes, and the plausible dislocation mechanisms driving incipient plasticity.
- **Chapter 5** concludes the thesis by summarising major findings and proposing future directions for research on orientation-dependent plasticity in Mg alloys.

Chapter 2 – Literature Review

2.1. Nanoindentation technique

Nanoindentation is a precise mechanical testing technique used to measure the hardness, elastic modulus, and other mechanical properties of materials at the nanoscale. By applying a controlled force using a sharp indenter, such as a Berkovich or spherical tip, and measuring the resulting penetration depth, nanoindentation provides insights into a material's response to localized deformation. This method is particularly valuable for studying thin films, coatings, and small volumes of material, where conventional hardness tests are impractical [16, 17]. Advanced analyses, such as load-displacement curves, enable the evaluation of additional parameters like plasticity, creep, and fracture toughness, making nanoindentation a powerful tool in materials science and engineering.

Nanoindentation is particularly well suited for investigating the incipient plasticity and dislocation nucleation, as its small indenter generates highly localized stress fields that enable close examination of regions free from preexisting lattice defects. By this capability, it provides clearer insight into the fundamental mechanisms governing the initial formation of dislocations. Moreover, nanoindentation allows for the application of controllable and complex loads [17-19] providing varying levels of stress triaxiality, enabling the extraction of quantitative information that closely resembles triaxial stress states present in polycrystals. This capability makes it ideal for examining the initiation processes of deformation modes, such as dislocation and twinning nucleation [14, 18, 20, 21]. It is important to emphasize that this thesis specifically focuses on the onset of plastic deformation, commonly referred to as incipient plasticity.

2.1.1. Load-displacement (P-h) curve

In nanoindentation, by pressing a sharp indenter, typically made of diamond, into the sample and carefully recording both the applied load and the penetration depth, researchers can generate a precise profile of how the material deforms under stress through the load-displacement (P-h) curve. From the P-h curve, key properties, such as hardness and elastic modulus can be extracted.

A typical P–h curve consists of an initial elastic deformation phase, followed by a plastic deformation phase, with a transition region in between where elastic and plastic behaviors coexist which is discussed in further sections. Figure 1 presents a schematic representation of the indentation process using a spherical indenter, along with the corresponding P–h curve, highlighting the elastic, plastic, and transition regions [16].

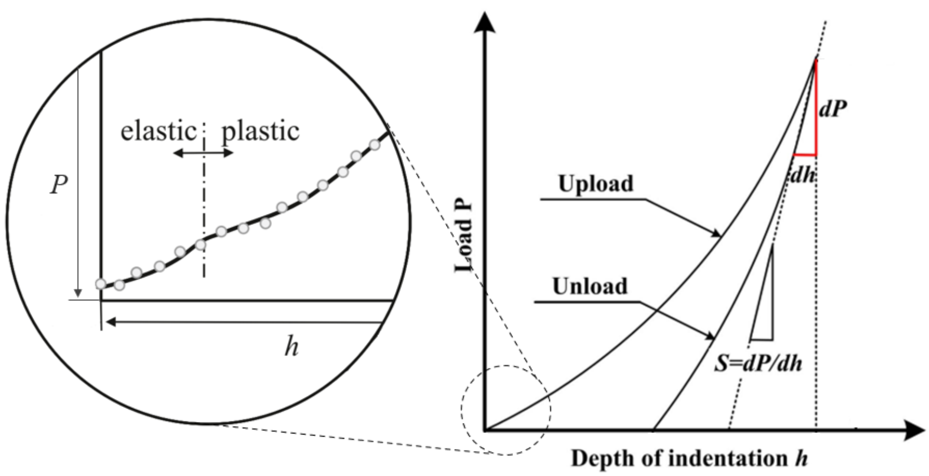

1Figure 2.1. a) Schematic of the Load-displacement curve after nanoindentation including the load, unload, elastic and plastic segments [16].

2.1.2. Elastic deformation behaviour

In the nanoindentation method, since a small indenter contacts the material at very localized scales and creates a highly concentrated stress field, the relationship between the applied load, the resulting displacement, and the underlying deformation processes can be understood by contact mechanics theory.

Due to the simplicity of modelling the elastic behavior in nanoindentation, the Spherical indenter is well-established and widely used in the literature [22].. The fundamental assumption is that two bodies—ideally spherical or with well-defined radii of curvature—experience purely elastic, frictionless contact, and isotropic[23, 24]. When a spherical indenter of radius R is pressed into a flat specimen under a load P, the contact forms a circular contact region with radius a. The magnitude of a depends on the applied load P and the effective elastic modulus E^* of the system, which accounts for the elastic moduli and Poisson's ratios of both the indenter and the sample. Mathematically, the relationships can be expressed as:

$$P = \frac{4}{3} E^* \sqrt{R^*} h_e^{3/2} \qquad \text{Eq. 2.1}$$

Where h_e is the penetration depth inelastic stage, and E^* and R^* are the effective modulus and effective radius given by:

$$\frac{1}{E^*} = \frac{1-\nu_s^2}{E_s} + \frac{1-\nu_i^2}{E_i} \qquad \text{Eq. 2.2}$$

Where ν_s and E_s are Poisson's ratio and Young's modulus of the specimen while ν_i and E_i are the diamond indenter's Poisson's ratio and Young's modulus ($\nu_i = 0.07$, $E_i = 1141$ GPa).

Under purely elastic contact on the unloading part, using a multiple-point unload approach, the slope of the initial portion of the unloading curve is described by [25]:

$$\frac{dP}{dh} = 2E^* R^{1/2} h_e^{1/2} \qquad \text{Eq. 2.3}$$

Since *S* is contact stiffness and given by the quantity *dp/dh*, and A is the area of contact given by πa^2, the Young's modulus can be obtained by:

$$E^* = \frac{\sqrt{\pi}\, S}{2\sqrt{A}} \qquad \text{Eq. 2.4}$$

By the using this model , a robust estimation of the sample's elastic behaviors can be obtained. While this work focuses on the spherical indenter, numerous other models have been developed in the literature to account for various indenter geometries, including conical, pyramidal, and flat punch tips [26-29]. As the load and displacement progress during a nanoindentation test, the material response transitions from purely elastic to plastic deformation [22]. Owing to the highly localized nature of nanoindentation—confined to a volume encompassing only a few atomic layers—the initial deformation typically occurs within a nearly defect-free lattice [30, 31]. Consequently, the onset of plasticity is generally associated with the nucleation of deformation modes such as dislocation and/or twining [32, 33]. This early-stage transition from elasticity to plasticity, commonly known as incipient plasticity, is discussed in detail in the following section.

2.1.3. Incipient plasticity in nanoindentation

As mentioned earlier, incipient plasticity is defined as the earliest stage of irreversible deformation [34, 35], typically involving the nucleation of deformation modes such as dislocation and/or twining [35, 36]. The incipient plasticity is often accompanied by a sudden displacement burst of a few nanometers under load-control conditions, commonly referred to as a “pop-in” or “first pop-in”. In displacement-control mode, the same phenomenon appears as a drop in the P-h curve [16, 17, 19]. In this chapter, for the explanation, we focused on load-control conditions for the sake of consistency, although we also included observations made under displacement-control conditions. The term “pop-in” refers to a distinguishable segment on the load–displacement (P–h) curve whose slope differs from that of the Hertzian fit. While a pop-in usually appears as a region of constant load (zero slope), it may sometimes exhibit a nonzero slope. Another key feature of a pop-in is that, once it occurs, the slope of the curve changes again, deviating from both the Hertzian fit and the initial pop-in slope. Although multiple pop-ins can appear on a nanoindentation curve, the term “incipient plasticity,” by definition, corresponds to the first pop-in event. The manifestation of pop-in signifies the activation of lattice-level mechanisms, such as dislocation or twinning nucleation, that accommodate the applied strain.

Pethica and Oliver [37] suggested that pop-in events are associated with sudden nucleation of dislocations, and the contact stress is close to the theoretical lattice strength when the surface is nearly defect-free. Numerous studies have reported shear stress values at pop-in ranging from G/10 - G/30, which support the occurrence of homogeneous dislocation nucleation [11, 20, 33, 38-43].

2.1.4. Shear stress at pop-in

To quantitatively evaluate the incipient plasticity stress, the maximum shear stress (τ_{max}) corresponding to the first pop-in event can be estimated according to the Hertzian elastic contact mechanics for spherical indentation on a defect-free surface [44, 45]. Based on this model, inside the circular contact area, the contact pressure distribution is assumed to be semi-ellipsoidal, with its highest value at the center (r=0), where r denotes the radial distance from the center of the circular contact area on the specimen's surface. The maximum contact pressure (P_0) is defined as [24]:

$$P_0 = (\frac{6PE_r^2}{\pi^3 R^2})^{1/3} \quad \text{Eq. 2.5}$$

The calculation of resolved shear stress on a specific plane and direction can be done by applying the Schmid factor concept. However, in a nanoindentation, since the stress field below the indenter is not uniaxial, it is often approximated by a triaxial compressive stress state, Li et al. [46] defined the indentation Schmid factor (ISF). The ISF is the ratio of the maximum resolved shear stress $\tau_{RSS}^{(\alpha)}$ on a given slip system (α) to the maximum contact pressure, P_0.

$$\tau_{RSS}^{(\alpha)} = ISF^{(\alpha)} \cdot P_0 \quad \text{Eq. 2.6}$$

The stress tensor (σ_{ij}) is used to capture the complete state of stress as expressed in the following equation [46]:

$$\tau_{RSS}^{(\alpha)} = s_i^{\alpha} \cdot m_j^{\alpha} \cdot \sigma_{ij} \quad \text{Eq. 2.7}$$

Where s_i^{α} and m_j^{α} represent the slip direction and slip plane normal of the slip system (α), respectively.

ISF is a dimensionless parameter, and its highest value is 0.31, therefore, the maximum shear stress corresponding to the elastic-plastic transition loads can be given by [24]:

$$\tau_{RSS}^{Max} = (3/2).ISF.P_m = 0.47P_0 \quad \text{Eq. 2.8}$$

2.1.5. Activation volume

As mentioned earlier, the first pop-in is recognised as an indicator of dislocation nucleation. The statistical nature of this event can be directly correlated to the activation volume associated with the first pop-in. Schuh et al. [47] developed a framework to relate the rate-dependent behavior of dislocation nucleation events observed during nanoindentation to the activation volume, providing a quantitative measure of the atomic-scale mechanisms at play. Activation volume, in this context, represents the effective volume swept by dislocations or associated with atomic-scale defect rearrangements during the thermally activated and stress dependent process of overcoming local energy barriers. By analyzing the probabilistic distribution of pop-in stress, an analytical model has been developed to determine the activation volume associated with the pop-in. Dislocation nucleation involves overcoming an activation barrier, which can be achieved through the mechanical work exerted by the indenter or the combined effects of thermal and mechanical work [47].

The nucleation rate per unit volume, denoted as η^0, is given by [47, 48]:

$$\eta^0 = \eta \exp(-\frac{\varepsilon - \tau V}{kT}) \qquad \text{Eq. 2.9}$$

In this context, η is the attempt frequency factor which presents the number of atomic tries at nucleation each second when no external stress is present ε is the activation energy barrier for the dislocation nucleation process, τ, is the maximum resolved shear stress generated beneath the spherical indenter is approximately 0.47 P_0, where P_0 is the maximum contact pressure, and V (activation volume) represents , the effective swept volume that couples the applied shear stress to the energy barrier. Thus, activation volume for the process with considering spherical indenter can be expressed as [47-49]:

$$V = \frac{\pi}{\left(\frac{3}{2}\right).ISF} \left(\frac{3R}{4E_r}\right)^{2/3} kT\alpha \qquad \text{Eq. 2.10}$$

Where, α is a time-independent parameter obtained from the linear fit of the slope of the ln(−ln(1−F)) versus $P^{1/3}$ plot. F denotes the cumulative probability that the first pop-in occurred by the specified load, and it provides the statistical link between the measured pop-in distribution and the activation-volume formulation..This statistical treatment of pop-in events was first introduced by Schuh et al. [47] for extracting V from nanoindentation experiments.

Analyzing the activation volume serves as a fundamental parameter to identify the controlling deformation mechanisms of nucleation during first pop-in. For instance, Schuh et al. [47] reported that, in single-crystal SiC, the activation volume for the first pop-in was less than $1b^3$ (where b is the Burgers vector), suggesting that such a small volume—only a few atomic volumes—may be linked to point-defect-assisted dislocation nucleation. Similarly, Manson et al. [50] observed in single-crystal Pt that the activation volume, roughly $0.5b^3$, is much smaller than one would expect for a conventional critical-sized homogeneous dislocation loop. They also found that the estimated activation energy was too low to be solely driven by ordinary thermal fluctuations, thereby proposing a vacancy-assisted mechanism for the first pop-in. Moreover, molecular dynamics simulations in various FCC metals have shown that vacancies can act as precursors, initiating dislocation nucleation [51]. Another proposed mechanism for pop-in, especially in high-entropy alloys (HEAs), involves solute-assisted dislocation nucleation, indicating that local compositional fluctuations may similarly promote or facilitate the early stages of plastic deformation [20, 43, 49, 52].

In addition, studies with uniaxial compression test on the single crystal Cu nanowire [53, 54] showed that surface-mediated dislocation nucleation is often characterized by a remarkably low activation volume, typically on the order of 1–10 b^3. Such small volumes imply that only a few atoms participate in creating the dislocation embryo at the free surface, leading to high sensitivity of the nucleation stress to both temperature and strain rate.

Although only a few studies have directly compared activation volumes from nanoindentation experiments with atomistic simulations to assess their reliability, the available evidence strongly supports the validity of the experimental results. Molecular dynamics (MD) simulations and embedded atom method (EAM) simulations [32, 55, 56] consistently show that the first pop-in event during nanoindentation corresponds to the nucleation of a dislocation loop, which is confined to just a few atomic distances—typically on the order of a few b [47, 50, 57] These simulation-derived volumes closely match the sub-10 b^3 activation volumes obtained from strain rate–dependent nanoindentation analysis, suggesting that the experimental approach captures the same fundamental atomistic process [12, 15, 47, 58].

2.2. Modes of pop-ins

According to the literature, pop-in in metals and alloys manifests in three primary modes:

(i) *Single pop-in:* A single pop-in appears immediately following the Hertzian fit.

(ii) *Successive pop-ins:* Multiple smaller pop-ins events occur progressively.

(iii) *Curve deviation before pop-in:* A slight deviation/excursion from the Hertzian fit is observed prior to the pop-in event.

Each mode signifies the onset of plastic deformation, albeit driven by distinct underlying mechanisms. The following sections will discuss these mechanisms in detail and elucidate how they influence incipient plasticity in different materials.

Figure 2 provides a schematic representation of the three distinct incipient plasticity modes.

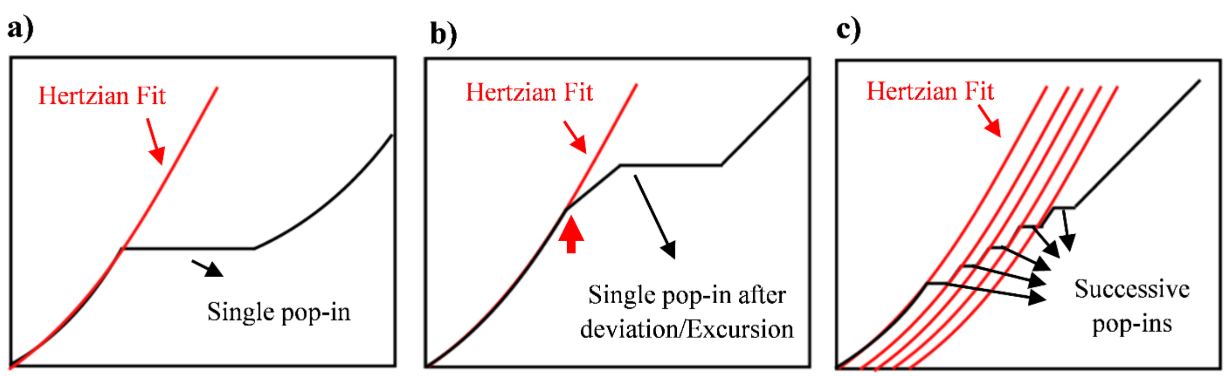

2Figure 2.2. Schematic illustration of three distinct modes of incipient plasticity. a) single pop-in, b) Successive pop-ins, c) Single pop-in after a slight deviation from Hertzian fit.

2.2.1. Single pop-in

According to the literature, this type of incipient plasticity reported in different metals and alloys [11, 43, 46, 50, 52, 59-65]. In this mode, the transition of the pure elastic regime changes to the plastic regime with the nucleation of deformation modes.

This pop-in occurs without any prior deviation from the Hertzian fit, indicating that the material remains elastically loaded right up to the threshold stress for dislocation nucleation. Experimental investigations by Oliver and Pharr [27] were among the first to document this phenomenon in metals such as tungsten, where a single, pronounced pop-in was observed shortly after the nanoindentation load was applied. Subsequent studies suggested that this is indicative of a homogeneous dislocation nucleation [50, 66-75], which is plausible given the minimal likelihood of encountering any preexisting dislocations [71] . Gouldstone et al. [59] investigated the underlying mechanism of this incipient plasticity mode by simulating nanoindentation in a two-dimensional defect-free single-crystal bubble raft. Their study demonstrated that this behavior originates from the sudden emergence of dislocation nucleation in a defect-free region beneath the indenter (approximately 0.48a, where a represents the contact area), where the stress distribution reaches its maximum level.

Molecular dynamics (MD) and embedded atom model (EAM) simulations elucidating the atomistic mechanisms responsible for these single pop-in events [56, 68]. By capturing atomic-scale processes, MD studies show how the contact stress intensifies beneath the indenter until it reaches a critical level, at which point a dislocation loop spontaneously forms and subsequently propagates, causing the observed displacement burst. These simulations also reveal that the stress required to trigger homogeneous dislocation nucleation often approaches a significant fraction of the material's shear modulus (on the order of G/10 to G/30) [32].

2.2.2. Curve deviation before pop-in

Another form of incipient plasticity reported in the literature is a pop-in event that follows a noticeable deviation from the Hertzian fit [32, 68, 76, 77]. The initial deviation during nanoindentation can manifest as a change in the slope of the load–displacement curve compared to the Hertzian fit.

Atomistic simulations of incipient plasticity in FCC metals such as Al, Cu, and Au during nanoindentation suggest that the initial deviation from elastic behavior originates from the nucleation dislocations at the free surface [68, 78-80]. This behavior is reported in Mg s HCP metal as well [15]. It is important to note that this type of pop-in does not always manifest as a clear deviation in the slope from the Hertzian fit; instead, it may appear as a subtle excursion from the Hertzian response prior to the first distinct pop-in event [32].

Needless to say, this deviation or small excursion has a very small length (around 1-2 nm) suggesting that plastic mechanisms begin to activate before the abrupt pop-in.

Li et al. [32] reported minor excursions (less than 2 nm) in the P-h curve prior to the main pop-in in Al(111) single crystals. Their MD simulation (Figure 3) demonstrated that this small excursion

(m) is attributed to the single slip event where just one prismatic loop is created at the surface, subtly modifying the P–h curve. On the other hand, the pop-in (M) which has a larger length compared to the excursion, is attributed to at least ten consecutive complete slips, happening underneath the indenter.

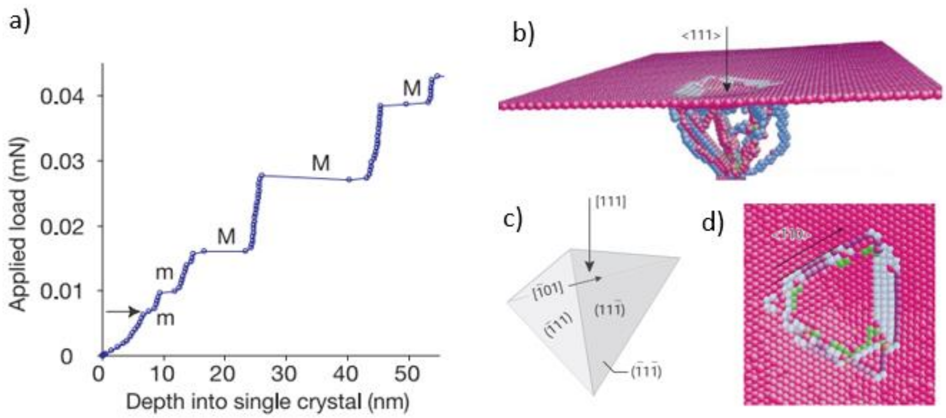

3Figure 2.3. a) P–h curve showing small excursion (m) and pop-in (M); b) MD simulation of a 12 nm spherical indenter on Al <111> surface showing sessile structure from glide loops on {111} planes [32].

These findings reinforce that incipient plasticity need not manifest as a single, isolated event; instead, it may initiate at lower stresses, producing a moderate but discernible deviation from purely elastic contact mechanics.

2.2.3. Successive pop-ins

In some cases, incipient plasticity manifests through multiple smaller pop-ins instead of a single pop-in. It is important to note that between these discrete events, the load–displacement curve often follows a Hertzian fit, indicating brief returns to elastic behavior. In other words, the atomic processes that accommodate the strain and generate each pop-in are interspersed with periods of purely elastic response, leading to successive pop-ins.

This type of incipient plasticity is mostly reported in FCC metals like Au, Al, Ni, and Cu [42, 59, 81-86]. Extensive simulations on Al, Ni, and Cu have demonstrated that successive pop-ins in FCC metals are closely linked to the formation of Lomer–Cottrell (L–C) locks [86]. The initial pop-in event corresponds to the nucleation of extended dislocations, while the subsequent elastic loading

phases allow these dislocations to propagate and interact, ultimately leading to the formation of L–C locks. Once these locks are established, the indentation response temporarily follows the Hertzian elastic fit until another extended dislocation nucleates, triggering the next pop-in event.
These L–C locks give rise to half-prismatic dislocation loops (half-PDLs), which are anchored at the surface, restricting their movement into the bulk of the crystal. However, as indentation progresses, additional extended dislocations form and align with the L–C Burgers vector, leading to the formation of closed prismatic dislocation loops (PDLs).
Figure 4 illustrates the simulation process of Lomer–Cottrell (L–C) lock formation, depicting the interaction of extended dislocations in each pop-in, the development of half-prismatic dislocation loops (half-PDLs), and their subsequent transition into fully closed prismatic dislocation loops (PDLs) in (111) orientation in the pure Cu [86].

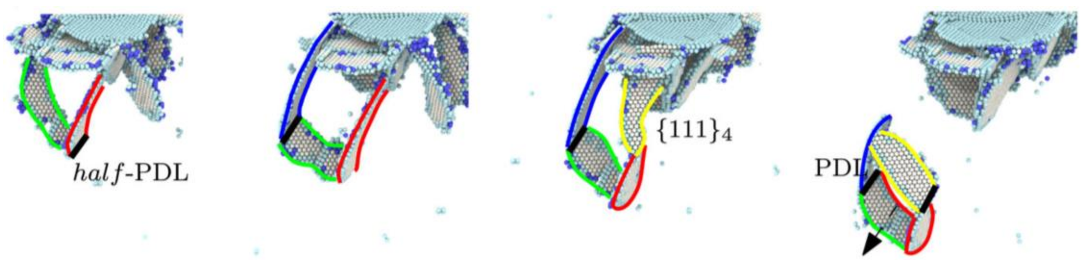

4Figure 2.4. Formation of Lomer–Cottrell locks in pure Cu (111) orientation, showing the transition from half-PDLs to fully closed PDLs during successive pop-ins from a) to d) [86].

Successive pop-in events have also been observed in BCC metals such as tungsten (W) [39, 44, 87]. Bahr et al. [44] reported that this “staircase” or successive pop-in phenomenon occurs only in the (111) orientation of tungsten, likely due to the limited number of dislocations in that orientation. In essence, the sample initially deforms elastically, and once the applied stress reaches the theoretical shear strength, a small number of dislocations nucleate. Because this number of dislocations is insufficient to sustain plastic flow, the stress quickly drops, allowing the material to elastically reload. When the stress again reaches a critical level, additional dislocation sources are activated, causing a repeated “pop-in” effect. This cycle continues until a sufficiently large dislocation network forms, enabling continuous plastic deformation.
There are several reports of successive pop-in events occurring in specific crystallographic orientations of HCP metals—particularly in basal orientations of magnesium in Mg[14, 15, 88].

Although it has been proposed that this behavior may originate from c-axis deformation mechanisms such as pyramidal dislocations [15] or twinning [88], it remains unclear whether these events represent multiple independent pop-ins or a sequence of successive pop-ins separated by elastic intervals. Moreover, no comprehensive statistical analysis or atomistic simulations have been conducted to explain the origin of such behavior in magnesium or other HCP metals. These three pop-in modes have been reported in various metals and alloys across a broad range of crystallographic orientations. However, due to the stochastic nature of pop-in events, statistical analysis is essential to reliably evaluate their orientation dependence. To the best of the authors' knowledge, no comprehensive statistical analysis has been conducted to determine the prevalence of specific pop-in modes as a function of crystallographic orientation. Therefore, a rigorous and statistically significant evaluation is needed to clarify the frequency and dominance of each mode across different orientations.

2.3. Orientation dependence of incipient plasticity

The incipient plasticity during nanoindentation is highly dependent on the crystallographic orientation of the tested material. This anisotropic behaviour arises from variations in dislocation nucleation stress, which can be effectively described by the Schmid factor.

Yao et al. [89] demonstrated a clear orientation dependence of pop-in loads in tungsten single crystals, where the (100) orientation exhibited the highest pop-in loads, followed by (110), with the lowest observed in (111). Similar trends have been reported in molybdenum and tantalum single crystals in other studies [90, 91]. The differences in pop-in load can be attributed to the variation in the Schmid factor, the (111) orientation has the highest Schmid factor, making it more susceptible to early dislocation nucleation and, consequently, lower pop-in loads. In contrast, the (100) orientation has a lower Schmid factor, requiring higher applied stress to activate dislocation motion.

In face-centred cubic (FCC) metals, however, the (111) orientation typically exhibits the highest pop-in load, indicating greater resistance to plastic deformation, while the (001) and (110) orientations show lower pop-in loads. This behaviour is primarily governed by the Schmid factor, which influences the ease of slip initiation under an applied load. The predominant dislocation system in FCC metals, $\langle 1\bar{1}0\rangle\{111\}$, has a Schmid factor of 0.27 for the (111) orientation. In contrast, for the (001) and (110) planes, the Schmid factor is 0.4, which is approximately 1.5 times higher than that of the (111) plane. This higher Schmid factor facilitates easier activation of glide systems in the (001) and (110) orientations [92, 93]. At the atomic scale, molecular dynamics (MD) simulations have confirmed that the primary mechanism governing the onset of plasticity in FCC metals is the nucleation of Shockley partial dislocations, regardless of crystallographic orientation [32, 94]. Furthermore, MD simulations show that partial dislocation nucleation occurs more readily in the (001) and (110) orientations, forming closed loops more easily compared to the (111) orientation [93]. This observation aligns with the higher Schmid factor values of the (001) and (110) orientations, which result in lower pop-in loads and easier slip activation.

In hexagonal close-packed (HCP) metals, such as magnesium (Mg), titanium (Ti), and hafnium (Hf), the c/a ratio plays a significant role in determining their anisotropic mechanical response [95]. The c/a ratio dictates the relative ease of slip activation in different orientations, leading to variations in plastic deformation behaviour. For instance, Mg, with a c/a ratio close to 1.633, primarily activates basal ⟨a⟩ dislocations, making basal slip the most favourable deformation mode [1]. In contrast, Ti, with a c/a ratio of 1.58, exhibits a deformation response dominated by prismatic ⟨a⟩ slip, which is the easiest slip system to activate [95]. Kwon et al. [96, 97] performed nanoindentation experiments on an α-Ti alloy to examine its plasticity onset behaviour. Their study revealed that indentation in the basal (0001) orientation resulted in higher pop-in loads, while prismatic $(1\bar{1}00)$ and pyramidal $(11\bar{2}0)$ orientations exhibited lower pop-in loads. This suggests easier dislocation nucleation and plasticity in these orientations. The observed behavior was attributed to the dominant slip system in each orientation. In the $(1\bar{1}00)$ and $(11\bar{2}0)$ orientations, the predominant dislocation types were basal ⟨a⟩ and prismatic ⟨a⟩ slip systems, which have lower critical resolved shear stresses (CRSS). In contrast, for the (0001) orientation, deformation was primarily governed by pyramidal ⟨c + a⟩ slip, which requires significantly higher stresses for activation, leading to increased pop-in loads. Similarly, Gao et al. [98] investigated the incipient plasticity of Hf single crystals through nanoindentation. Their findings demonstrated that the c/a ratio has a significant impact on the indentation Schmid factor, particularly when the indentation direction deviates from the c-axis by more than 30°. This variation is attributed to a combination of elastic anisotropy and the c/a ratio, which influence the stress distribution beneath the indenter. Their experiments also confirmed that pop-in loads were highest for orientations near the c-axis, consistent with findings in Ti. A similar trend has been observed in magnesium nanoindentation studies [11, 14], where indentation along the c-axis resulted in higher pop-in loads compared to the $(10\overline{1}2)$ and $(10\overline{1}0)$ orientations. However, unlike previous studies on NiAl, where a strong correlation between the indentation Schmid factor and pop-in loads was established, experimental results for HCP metals do not exhibit the same level of agreement. This discrepancy was also noted by Barret et al. [99], who used MD simulations and uniaxial Schmid factor analysis to demonstrate inconsistencies in pyramidal dislocation nucleation.

These findings suggest that homogeneous dislocation nucleation during nanoindentation in HCP metals is not governed by a single slip system. Instead, it is influenced by a combination of basal ⟨a⟩, prismatic ⟨a⟩, and pyramidal ⟨c + a⟩ slip systems, with their relative contributions depending on the zenith angle of indentation. While indentation Schmid factor calculations provide useful insights into the orientation dependence of incipient plasticity, the actual mechanisms of plasticity onset are much more complex. Understanding the orientation dependence of incipient plasticity requires experimental testing on a wide range of crystallographic orientations. However, producing large, high-quality single crystals necessitates specialized equipment—such as Bridgman or Czochralski furnaces—and extremely slow solidification rates. Even laboratory-scale specimens demand substantial capital investment and consumables, while commercially available magnesium is almost exclusively polycrystalline[100]. Micromechanical methods, such as focused ion beam (FIB) fabrication of micropillars, mitigate the need for large single crystals but are very time-consuming and expensive [101]. As a result, experimental investigations covering a comprehensive range of orientations remain limited. Bridging this gap is crucial for advancing our understanding of orientation-dependent incipient plasticity.

2.4. Incipient plasticity in magnesium and its alloys

Magnesium (Mg) is a promising lightweight structural material, widely valued for its high strength-to-weight ratio and environmental benefits, making it an attractive choice for automotive, aerospace, and other industries aiming to reduce carbon emissions [1, 3, 4, 14, 15]. However, the widespread adoption of Mg alloys is hindered by their pronounced anisotropic plasticity, which limits their formability and mechanical performance in diverse applications [7, 8]. This anisotropy arises from the inherent crystallographic characteristics of the hexagonal close-packed (HCP) structure of Mg, where the activity of deformation modes is highly directional.

The primary deformation mechanisms in Mg include dislocation slip and twinning, with basal dislocation slip ($\{0001\}\langle 11\bar{2}0\rangle$ and extension twinning ($\{10\bar{1}2\}\langle 10\bar{1}1\rangle$ being the most active under typical loading conditions due to their relatively low critical resolved shear stresses (CRSS). In contrast, other deformation modes such as prismatic ($\{10\bar{1}0\}\langle 11\bar{2}0\rangle$ and pyramidal-I ($\{11\bar{2}2\}\langle 11\bar{2}3\rangle$) and pyramidal-II ($\{11\bar{2}2\}\langle 11\bar{2}3\rangle$) slip systems require significantly higher CRSS, resulting in limited contributions to overall plastic deformation. The dominance of basal slip and extension twinning, combined with the suppression of non-basal slip systems, underpins the strong anisotropy in Mg's plastic response [1].

Addressing this anisotropic behavior requires a fundamental understanding of the mechanisms governing incipient plasticity, specifically the nucleation of dislocations and twins. These processes dictate the onset of plastic deformation and play a pivotal role in determining the mechanical performance of Mg alloys under varying loading conditions. By elucidating the nucleation mechanisms of these deformation carriers, researchers can develop strategies to engineer Mg alloys with balanced deformation modes, thereby mitigating anisotropy and unlocking their full potential as high-performance structural materials.

Since incipient plasticity involves the nucleation stage of deformation mechanisms, the dislocation and twinning nucleation in magnesium and its alloys are reviewed in the following subsections.

2.4.1. Dislocation nucleation

Catoor et al. [11] investigated the incipient plasticity of pure Mg using spherical nanoindentation on three crystallographic orientations: (0001), $(10\bar{1}2)$, and $(10\bar{1}0)$. Their study revealed that, regardless of the indentation orientation, the pop-in events predominantly appeared in single pop-in mode, signifying a well-defined transition from elastic to plastic deformation. By performing statistical analysis of pop-in loads and calculating the resolved shear stress at pop-in, they demonstrated that the normalized shear stresses at the onset of plasticity was 0.6-1.2 GPa which closely matched the theoretical strength required for basal dislocation nucleation. This confirmed that pop-in is associated with homogeneous dislocation nucleation rather than pre-existing defect activation, twinning, or non-basal slip. Notably, this range of stress for dislocation nucleation in magnesium has been independently corroborated in molecular dynamics (MD) simulations, reinforcing the theoretical basis of their findings [99].

Their cross-sectional TEM analysis before and after indentation provided direct experimental evidence that dislocations nucleate during indentation. In all tested orientations, basal dislocations were found to be the dominant deformation mode under the indenter, despite the presence of other deformation mechanisms. Although extension twins ($\{10\bar{1}2\}\langle 10\bar{1}1\rangle$) were observed in the ($10\bar{1}2$) and ($10\bar{1}0$) orientations, the overwhelming presence of basal dislocations suggested that twinning occurs only during post-pop-in deformation, rather than initiating the plasticity event. This is a crucial distinction, as twinning is often a dominant deformation mechanism in larger-scale Mg deformation but appears to play a secondary role in incipient plasticity under nanoindentation [102-104].

Furthermore, Catoor et al. [11] utilized anisotropic contact mechanics to compute the Indentation Schmid Factor (ISF), a key parameter determining which slip system is most likely to be activated. Their analysis showed that for (0001) indentation, although pyramidal <c + a> slip ($\{11\bar{2}2\}\langle 11\bar{2}3\rangle$) had the highest ISF, the significantly higher self-energy of these dislocations made their nucleation unlikely. Instead, the activation energy barrier for basal dislocations was lower, enabling their preferential nucleation during pop-in. This observation aligns with theoretical predictions that incipient plasticity in Mg is governed by basal slip due to its relatively lower critical shear stress compared to prismatic and pyramidal slip [1].

Somekawa et al. [15] conducted a detailed investigation into the mechanisms of dislocation nucleation in both basal and prismatic orientations of pure magnesium, providing deeper insights into the incipient plasticity of this material. Their study, which combined nanoindentation experiments with molecular statics simulations, demonstrated that plasticity in Mg initiates with the nucleation of basal ⟨a⟩ dislocations at the surface. However, since these dislocations nucleate in a semi-loop (bow-like) shape, they contribute minimally to strain accommodation and primarily manifest as a deviation from the Hertzian elastic fit in load-displacement curves.

For indentation along the basal orientation, as the indentation depth increases, basal dislocations expand but eventually reach a limitation in their ability to accommodate further plastic strain. To relieve the increasing strain along the c-axis, basal dislocations cross-slip onto pyramidal planes, transitioning into pyramidal ⟨c+a⟩ dislocations ($1/3\langle 11\bar{2}3\rangle$ slip). This transition occurs when the screw components of basal dislocations rotate onto pyramidal planes, where they continue to glide. Since pyramidal ⟨c+a⟩ slip has a much higher CRSS, its activation requires higher stress, explaining the higher pop-in loads observed during nanoindentation on the basal plane compared to the prismatic plane.

For indentation along the prismatic orientation, the simulations revealed a similar initial nucleation of basal dislocations at the surface. However, instead of transitioning to pyramidal ⟨c+a⟩ slip, the basal dislocations cross-slip onto prismatic planes, activating prismatic ⟨a⟩ slip ($1/2\langle 11\bar{2}0\rangle$). This transition allows further deformation along the ⟨a⟩ directions within $\{10\bar{2}0\}$ prismatic planes. Their results align with those of Catoor [11], demonstrating that the early stage of incipient plasticity is dominated by basal dislocations. However, the activation of pyramidal dislocations at larger displacements accounts for the higher pop-in stress. Similarly, for indentation on the prismatic plane, prior studies consistently emphasize the critical role of dislocations with the <a> component in initiating plasticity. Figures 5 and 6 depict the atomic configurations during indentation in different stages in basal and prismatic orientations, respectively.

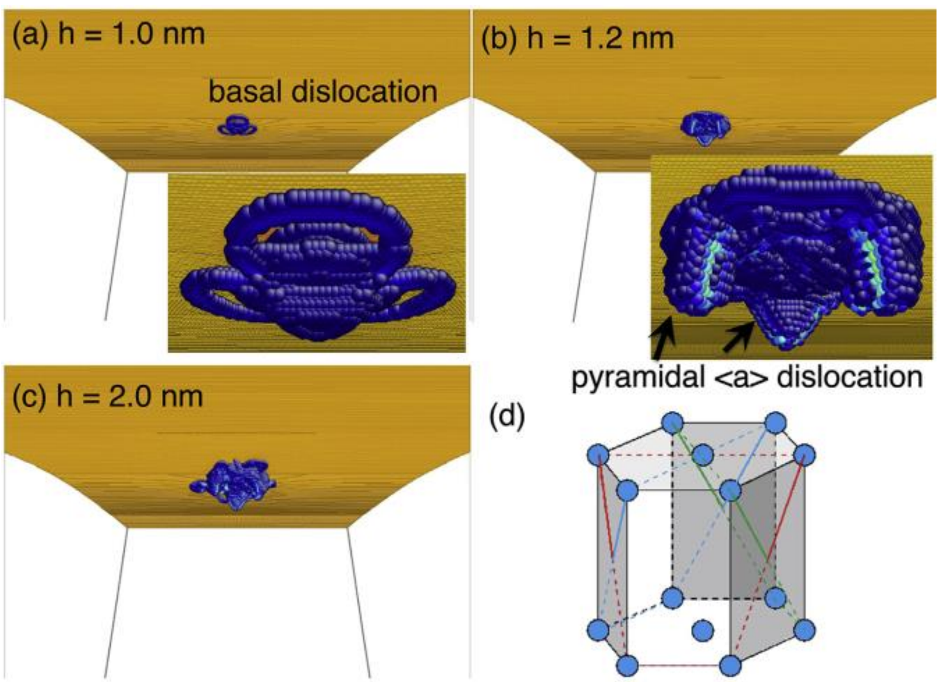

5Figures 2.5. Atomic configurations of incipient plasticity during indentation in different steps in basal orientation [15].

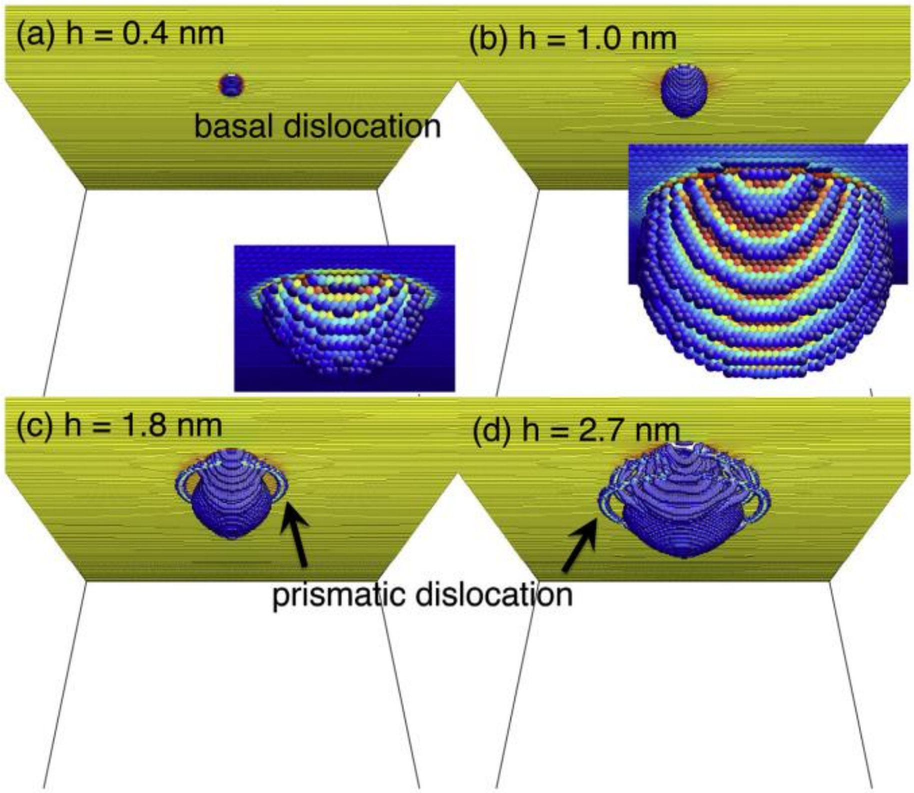

6Figures 2.6. Atomic configurations of incipient plasticity during indentation in different steps in prismatic orientation [15].

Recently, Goswami et al. [105] conducted embedded-atom method simulations to investigate the early incipient plasticity of magnesium crystals oriented with the c-axis normal to the indentation surface up to a depth of 20 Å. Their findings revealed that dislocation nucleation initiates at the contact surface in the form of "U-shaped" half loops, expanding in various directions. As these dislocations propagate, they coalesce to form prismatic loops—a process that occurs nearly simultaneously with dislocation nucleation. This orientation-dependent insight underscores the fundamental mechanisms of plastic deformation at the early stages of indentation and highlights the importance of crystallographic orientation in governing dislocation behavior in magnesium.

2.4.2. Twinning nucleation

Nayeri et al. [106] investigated the nanoindentation behavior of high-purity magnesium (Mg) with a (0001) crystallographic orientation. Their findings indicate that incipient plasticity is marked by an initial deviation from Hertzian elastic behavior, followed by multiple pop-ins during subsequent plastic deformation.

Through 3D-EBSD misorientation mapping, they demonstrated that the majority of residual dislocations beneath the indent are basal ⟨a⟩ dislocations, which is consistent with the last reported experiments and simulations [11, 15]. Furthermore, their analysis revealed that the first pop-in event corresponds to the nucleation of $\{10\bar{1}2\}$ extension twins. At greater indentation depths (≥500 nm), twinning becomes more pronounced, as evidenced by 3D-EBSD observations of twin structures adjacent to the indent. The successive pop-ins observed in the load-displacement curves correspond to the sequential activation of different twin variants, each forming at distinct stress levels, leading to multiple discontinuities in the loading curve. These results align with recent experimental and simulation studies on twinning nucleation, which indicate that a larger activation volume is required for its initiation. Specifically, the findings reveal that the nucleation of twinning involves the participation of at least six atomic layers [10].

Cheng et al. [12] conducted nanoindentation experiments on pure Mg in the $(10\bar{1}0)$, $(1\bar{2}10)$, and (0002) orientations, showing that pop-in events occurred following a deviation from the Hertzian elastic fit. For the $(10\bar{1}0)$ and $(1\bar{2}10)$ orientations, this deviation was linked to basal slip, as confirmed by slip traces observed around the indentation sites using atomic force microscopy (AFM). The subsequent pop-in events were attributed to the activation of extension twinning. In contrast, indentation on the (0002) orientation showed no evidence of basal dislocations or twinning at the surface. This led the authors to propose that, in this orientation, the onset of plasticity is governed by the nucleation of pyramidal ⟨c+a⟩ dislocations rather than basal slip or twinning. Further supporting this hypothesis, the calculated resolved shear stress (RSS) for (0002) indentation was found to be approximately twice as large as that for the $(10\bar{1}0)$ and $(1\bar{2}10)$ orientations. Additionally, the higher indentation Schmid factor (ISF) for pyramidal ⟨c+a⟩ slip provided further evidence that basal slip alone was insufficient to accommodate the induced strain. While the absence of surface traces of twinning or basal slip does not definitively rule out their occurrence beneath the surface, the findings are consistent with prior studies [47], which also suggest that plasticity in this orientation is likely dominated by pyramidal ⟨c+a⟩ dislocation activation. Figure 7 presents the P–h curve alongside AFM images of the surface for each orientation.

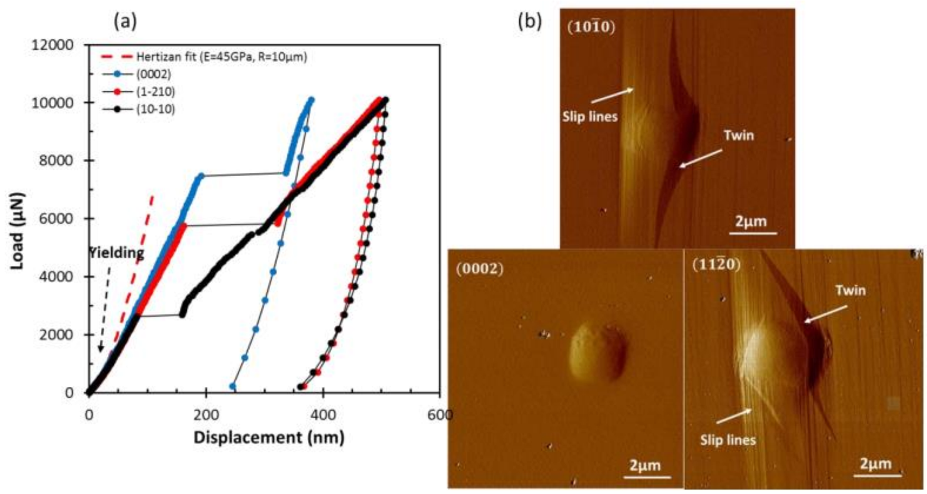

7Figure 2.7. Nanoindentation behaviors on pure Mg in different crystallographic orientations, a) P-h curves, b) corresponding AFM images of indenter impressions [12].

Guo et al. [107] reported dislocation initiation and twinning nucleation in Mg-Gd and Mg-Zn alloys during the nanoindentation technique with AFM in (10$\bar{1}$0) and (1$\bar{2}$10) crystallographic orientations [107, 108]. They linked the deviation of curve from Hertzian fit to the basal dislocation activation which is supported by the basal slip line on the surface. Moreover, pop-in event was attributed to the twinning nucleation based on the observation of twining traces on the surface. The Crystal Plasticity Finite Element Method (CPFEM) simulations were used to estimate the maximum resolved shear stress (RSS) on the {10-12} twinning system, showing that the stress matched the critical value for twin initiation and correlated precisely with the experimentally observed pop-in events.

Although the presence of solute atoms had a different effect of strengthening the initiation of dislocation and twinning, the trend of nucleation remained the same as pure magnesium. This trend was also observed in the study by Somekawa et al. [15], which investigated the incipient plasticity of Mg alloys containing Li, Al, Zn, and Y with small loading. The dislocation nucleation mechanism associated with pop-in was found to have an activation volume on the order of 0.2–1 b^3 and was minimally influenced by solute content [41].

In summary, the literature consistently demonstrates that the incipient plasticity in magnesium is initiated by basal dislocation nucleation. In the basal orientation, these basal dislocations act as precursors that subsequently transition to pyramidal <c+a> dislocations with increased loading.

Similarly, in the prismatic orientation, incipient plasticity is also governed by basal dislocations at the early stages, followed by a transition to prismatic <a> dislocations under further loading. Twinning has also been reported to nucleate in the basal orientation; however, its activation requires a larger activation volume. Therefore, distinguishing between dislocation slip and twinning during incipient plasticity is a critical aspect of understanding the contribution of each mechanism. This issue is further discussed in the following section. Moreover, while it has been determined that the presence of solute atoms does not fundamentally alter the sequence of dislocation and twinning nucleation, it does cause subtle shifts in the stress levels at which these events occur.

2.4.3. Decoupling the dislocation and twinning nucleation through the nanoindentation:

To decouple twinning and dislocation in incipient plasticity, it is essential to consider the volume of material required for each nucleation event. Twinning demands a significantly larger activation volume compared to dislocation nucleation. As previously discussed, atomistic simulations and experimental studies have shown that nucleation of a deformation twin requires activation across at least six atomic layers [10]. Moreover, Nayeri et al. [106] observed that twin nucleation in the basal orientation occurs only after the indenter has penetrated more than 500 nm. In contrast, dislocation nucleation—particularly the nucleation of partial dislocations from a free surface—can occur with far fewer atoms, sometimes involving as few atomic layers [32]. This fundamental difference forms the basis for distinguishing their occurrence during nanoindentation. From the nanoindentation side, instrument parameters must be chosen to limit the indented volume beneath the tip, which enhances the ability to distinguish between dislocation slip and twinning. The two most critical parameters are the indenter tip radius and the applied load. A smaller tip radius reduces the contact area and thus minimizes the deformed volume. Moreover, a lower indentation load limits the maximum displacement, further reducing the indented volume. It is important that using low loads improves the resolution of the load–displacement (P–h) curve, which helps identify subtle events such as early dislocation nucleation. However, the load must not be reduced below the noise threshold of the instrument, as it would obscure meaningful deviations in the P–h curve. Therefore, using a small-radius indenter and optimized low-load conditions is essential for focusing specifically on dislocation-dominated incipient plasticity and distinguishing it from twinning.

A notable example of this approach is the study by Guo et al. [103], who performed nanoindentation on magnesium using a spherical indenter with a 5 µm radius. They varied the applied load and examined post-indentation features using Atomic Force Microscopy (AFM). At lower loads (1.5–2 mN), they observed only slip lines, indicating basal dislocation activity. At higher loads (3–5 mN), twin boundaries became visible. Their results were further supported by Electron Backscatter Diffraction (EBSD), which confirmed that the slip lines corresponded to basal planes, and the newly formed boundaries were consistent with {10-12} tensile twins.

2.5. Gaps and challenges in study the Mg's incipient plasticity

Despite significant progress in understanding the incipient plasticity of magnesium and its alloys, several gaps and challenges remain. Nanoindentation studies on magnesium have primarily focused on low indexed basal, prismatic, and pyramidal orientations, consistently reporting that the basal orientation exhibits higher pop-in loads than the other two. However, the limited number of studied orientations has left gaps in the comprehensive understanding of the orientation-dependent mechanical response of magnesium. Expanding the range of crystallographic orientations examined in nanoindentation experiments is essential to developing a more complete picture of the anisotropic plasticity in magnesium and its alloys.

One of the primary experimental challenges in studying the orientation-dependent incipient plasticity of magnesium is the difficulty of preparing single-crystal magnesium specimens with precise crystallographic orientations. Producing high-quality single crystals in different orientations is not only experimentally demanding but also highly expensive. This limitation restricts systematic investigations across a broader range of orientations. Therefore, alternative approaches are required to facilitate the study of incipient plasticity in magnesium with greater accuracy and efficiency.

Addressing these gaps and challenges will be essential for advancing the understanding of magnesium's fundamental deformation mechanisms. A more comprehensive investigation of its orientation-dependent incipient plasticity could provide valuable insights for optimising the mechanical performance of magnesium alloys, particularly for applications in lightweight structural materials where strength, ductility, and plasticity control are critical.

2.6. Research Objective

To address the existing gaps and challenges in the understanding of incipient plasticity in magnesium, this study is designed with the following objectives:

1. *Nanoindentation experimental optimisation for studying the incipient plasticity in a broad range of crystal orientations in a Mg-Gd alloy:* Given the challenges associated with preparing single-crystal magnesium specimens in multiple orientations—and the resulting gaps in our understanding of orientation-dependent incipient plasticity—this objective focuses on optimizing nanoindentation techniques to capture the earliest stages of plastic deformation, with an emphasis on dislocation-mediated mechanisms. Key advancements include precise load control for detecting subtle pop-in events and the implementation of a grain orientation identification and targeting approach using nanoindentation combined with EBSD. This methodology enables the systematic investigation of a broad range of crystallographic orientations without relying on costly and difficult-to-fabricate single-crystal specimens.
2. *Study the orientation dependence of dislocation-induced incipient plasticity in the Ma-Gd alloy:* This objective aims to examine how varying crystal orientations influence the critical stress, pop-in behavior, activation volume, and underlying dislocation mechanisms governing incipient plasticity. By establishing a reliable and efficient framework for studying dislocation-mediated incipient plasticity, this objective aims to expand current knowledge beyond conventionally studied orientations and provide a foundation for a more comprehensive understanding of magnesium's anisotropic mechanical behaviour.

By addressing these objectives, this study aims to fill critical gaps in experimental data and establish a reliable methodology for investigating incipient plasticity using instrumented nanoindentation. It will enhance our understanding of dislocation nucleation mechanisms in magnesium, clarify the orientation dependence of incipient plasticity in Mg alloys, and contribute valuable insights to the broader field of plasticity in HCP metal

Chapter 3 - Materials, Experimental optimization and design, and Methodology

To minimize or suppress twinning, experimental conditions must rely on extremely low indentation volume, requiring precise control over indentation parameters, including small displacements and loads.

Moreover, to investigate orientation-dependent of dislocation-mediated incipient plasticity, high-quality single crystals in various orientations is needed. The preparation of high-quality single crystals in various orientations is both experimentally demanding and expensive Therefore, in this chapter, we present the experimental optimization for studying dislocation-mediated incipient plasticity and the proposed methodology for conducting experiments across different crystallographic orientations. We detail the critical parameters that were fine-tuned, including sample preparation procedures, load selection, scanning probe microscope optimization, and post-indentation surface analysis to assess the potential for twinning. Additionally, the proposed approach for grain location identification, essential for ensuring high-fidelity measurements, is thoroughly explained.

Figure 3.1 presents a comprehensive flowchart outlining the experimental design, optimization strategies, and overall methodology employed in this study.

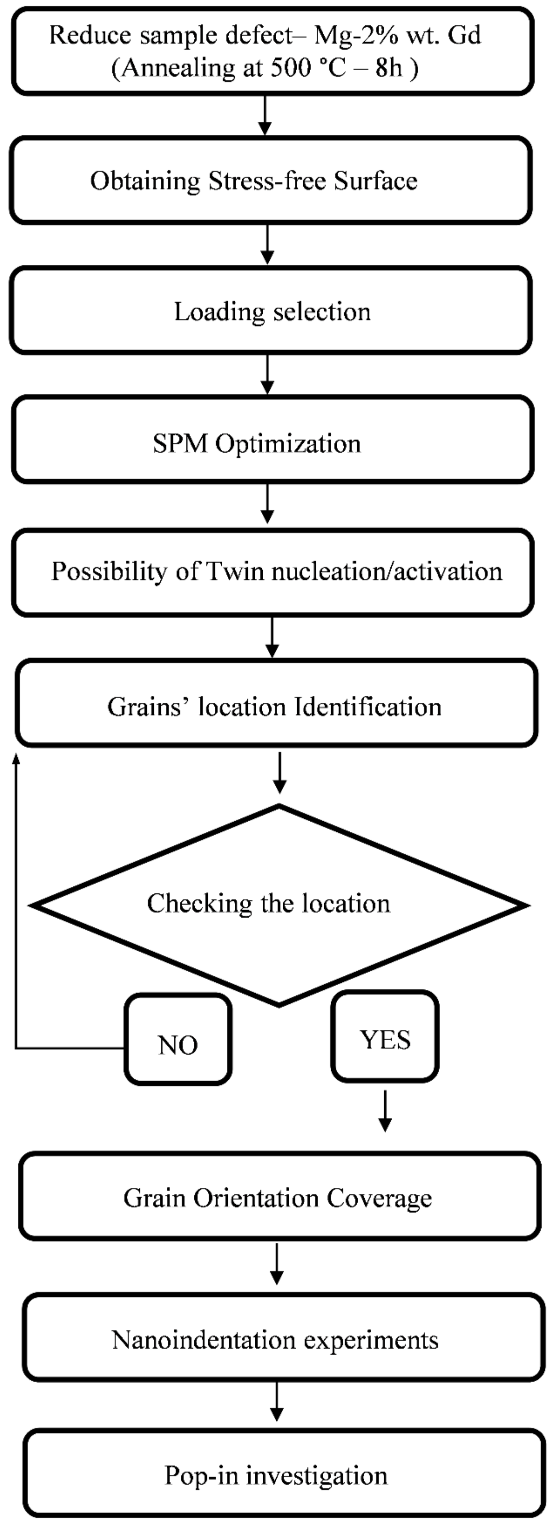

8Figure 3.1. A comprehensive flowchart outlining the experimental design, optimization strategies, and overall methodology employed in this study.

3.1. Material

In this study, a coarse-grained Mg–2 wt.% Gd alloy rod with dimensions of ϕ10 × 20 mm was used, as shown in Figure 3.2(a). The alloy was synthesized in an electric furnace by melting high-purity Mg (99.99%) with a Mg–25 wt.% Gd master alloy under an SF_6/CO_2 protective gas mixture. A solution treatment at 500°C for 8 hours was performed, resulting in coarsened grains and the reduction of crystal defects [109]. Although this treatment is crucial for minimizing defects, it can cause excessively large grains in pure Mg. Gadolinium (as a rare-earth element) was introduced to help prevent such excessive grain growth by segregating at grain boundaries [110]. Figure 3.2(b) schematically illustrates how the samples were sectioned from the cylinders, and Figure 3.2(c) shows the Mg–2.0 wt.% Gd sample mounted on the holder for EBSD and nanoindentation tests.

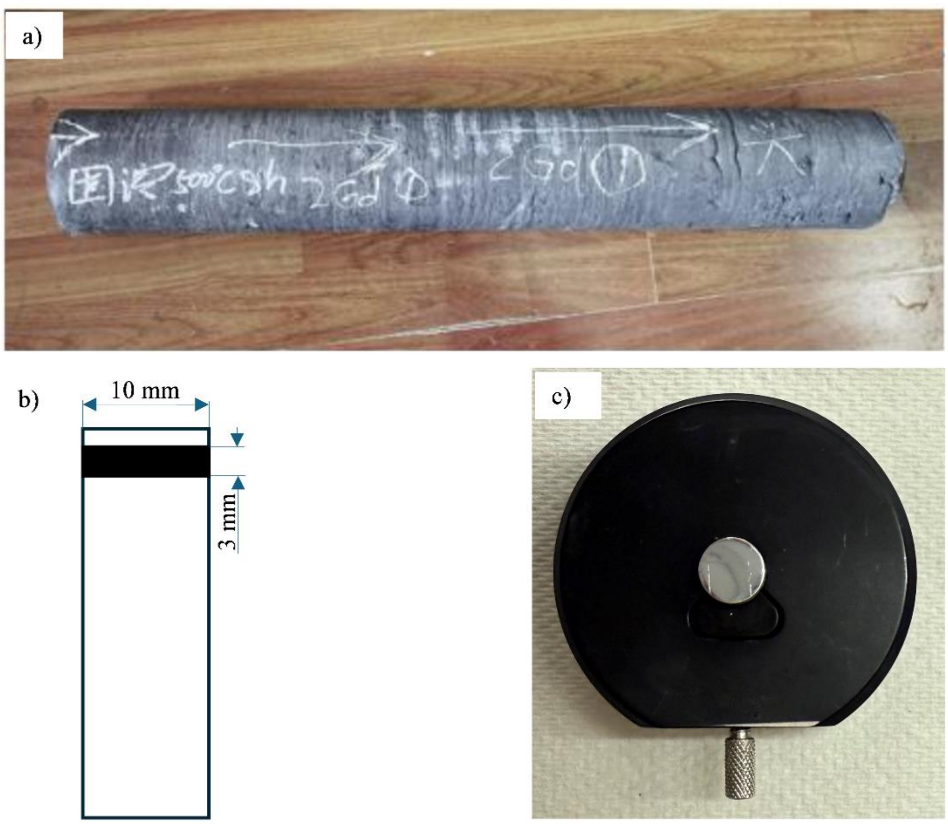

9Figure 3.2. Illustration of the (a) Mg-Gd (2.0 wt.%) binary alloy ingot; (b) schematic illustration of how the sample was cut from the raw ingot, (c) sample located on the holder for EBSD and nanoindentation experiments.

To measure the average grain size, three EBSD maps containing various grain orientations were selected, as shown in Figure 3.3. The average grain size, determined via the intercepts method in

OIM software, was 215 µm . Due to the large variation in grain sizes, only grains larger than 200 × 200 µm were selected for subsequent experiments to minimize grain boundary effects.

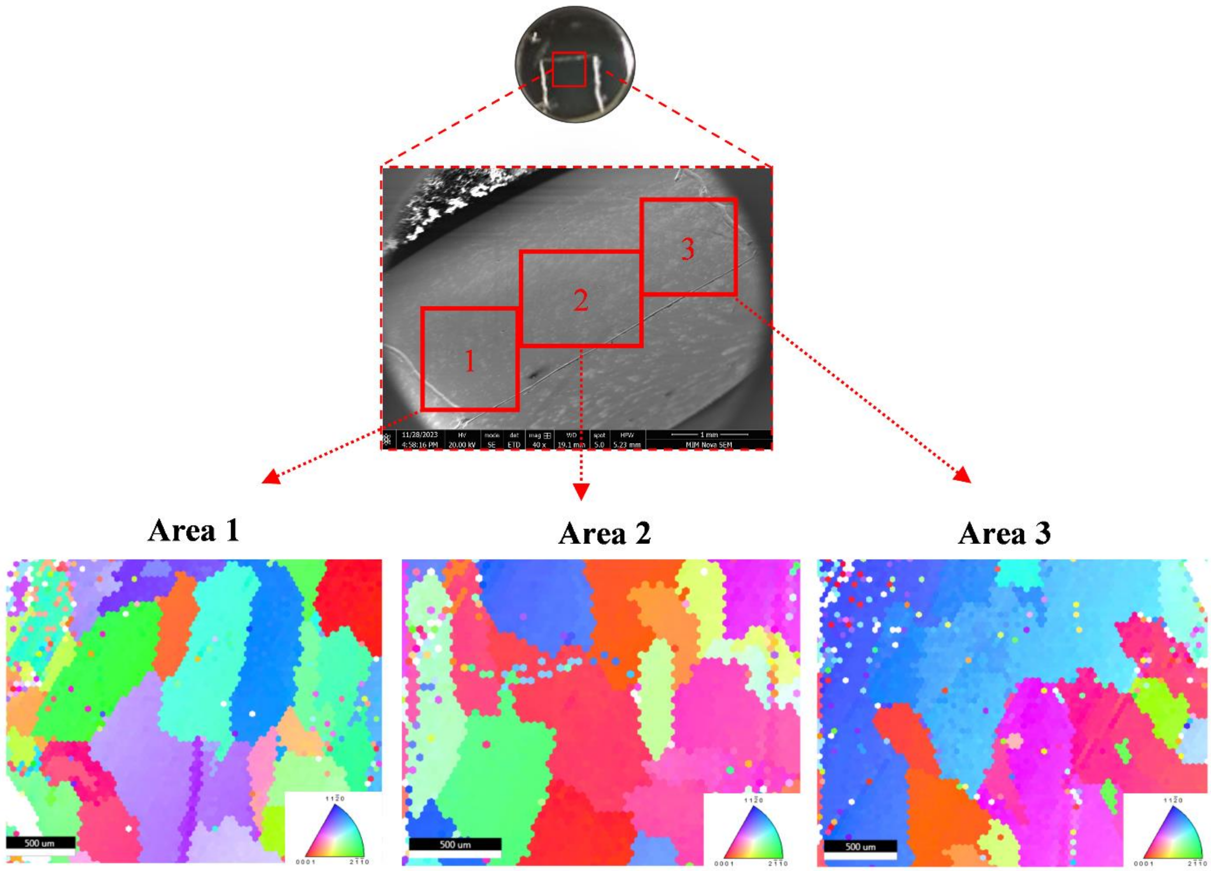

10Figure3.3. EBSD maps of three selected regions used to measure the average grain size.

3.2. Surface preparation

Accurate grain orientation analysis using the electron backscatter diffraction (EBSD) technique requires that the sample surface be both stress-free and extremely smooth. Any residual stress or surface roughness can distort the diffraction patterns and reduce the confidence index during orientation mapping. Furthermore, during nanoindentation testing, the initial "pop-in" events—commonly observed as abrupt displacement excursions—are highly sensitive to subtle variations in surface condition. Consequently, achieving a mirror-like finish is critical for minimizing measurement artifacts and enhancing the reliability of both EBSD and nanoindentation data.

3.2.1. Mechanical polishing

The samples were first ground using sandpapers with grit sizes of 600, 1200, and 4000. This step helped to remove any major surface irregularities and gradually reduce surface roughness. Subsequent mechanical polishing was carried out using a MultiPrep™ machine with a polishing cloth, employing polycrystalline glycol-based suspensions containing diamond particles of 3, 1, 0.25, and 0.05 μm, along with a 0.05 μm silica suspension from Allied. During polishing, a rotational speed of 300 r.p.m. was maintained to obtain a mirror-like finish. To ensure consistent results, samples were thoroughly cleaned (e.g., rinsed with ethanol and dried) after each polishing stage to eliminate debris from previous steps.

3.2.2. Electron backscatter diffraction (EBSD) maps

To identify different grain orientations in materials, an FEI Nova NanoSEM 450 equipped with an EBSD detector was used. The EBSD maps were post-processed using orientation imaging microscopy (OIM) analysis software (TSL OIM analysis 7.3, EDAX Inc., USA). During data acquisition, samples were typically tilted at 70° relative to the electron beam to optimize pattern detection, and appropriate accelerating voltages (e.g., 15–20 kV) and working distances were 5mm to achieve clear Kikuchi patterns. Figure 3.3 illustrates an EBSD map from the sample surface, showing various grain orientations represented through an inverse pole figure (IPF).

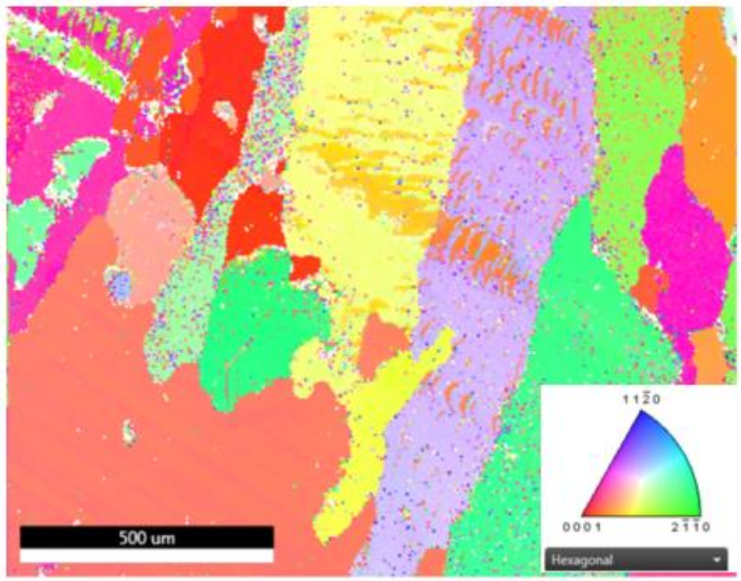

11Figure. 3.4. Different grain orientations in EBSD with the inverse pole figure (IPF) image.

3.2.3. Obtaining stress-free surface

The initial surface preparation involved grinding the sample using sandpapers with 600, 1200, and 4000. Subsequent mechanical polishing was conducted with a MultiPrep™ machine, utilizing various polycrystalline glycol-based suspensions containing diamond particles of 3, 1, 0.25, and 0.05 µm, and a 0.05 µm silica suspension. The 3 and 1 µm diamond suspensions were applied for 30 minutes each, while the final polishing with 0.05 µm diamond particles and 0.04 µm silica particles was carried out for 2 hours. The etching process employed a solution composed of 4 ml HNO_3, 6.5 ml HCl, and 100 ml ethanol [12]. The quality of the surface preparation was assessed using the confidence index (CI), which is the ratio of indexed bands to total bands in electron backscatter diffraction (EBSD) [111] through a FEI Nano Nova SEM instrument equipped with an EBSD detector. Our results indicate that etching, commonly used for Mg alloys (4 ml HNO_3 + 6.5 ml HCl + 100 ml ethanol) [112, 113], yielded inferior EBSD signals compared to a single step of mechanical polishing. Moreover, using a suspension with finer particles results in a smoother surface with a higher confidence index (CI) during EBSD signal collection. Furthermore, between silica and diamond 0.05 µm particle size suspensions, the diamond particle suspension resulted in a higher CI after 2 hours of mechanical polishing, providing a smoother surface. Figure 3.4 illustrates different EBSD maps from various polishing conditions, including the use of diamond particle and silica particle suspensions with and without final etching. As shown, the highest CI is

0.58, achieved by polishing with a polycrystalline diamond glycol-based suspension with 0.05 μm particle size, which we selected for our study.

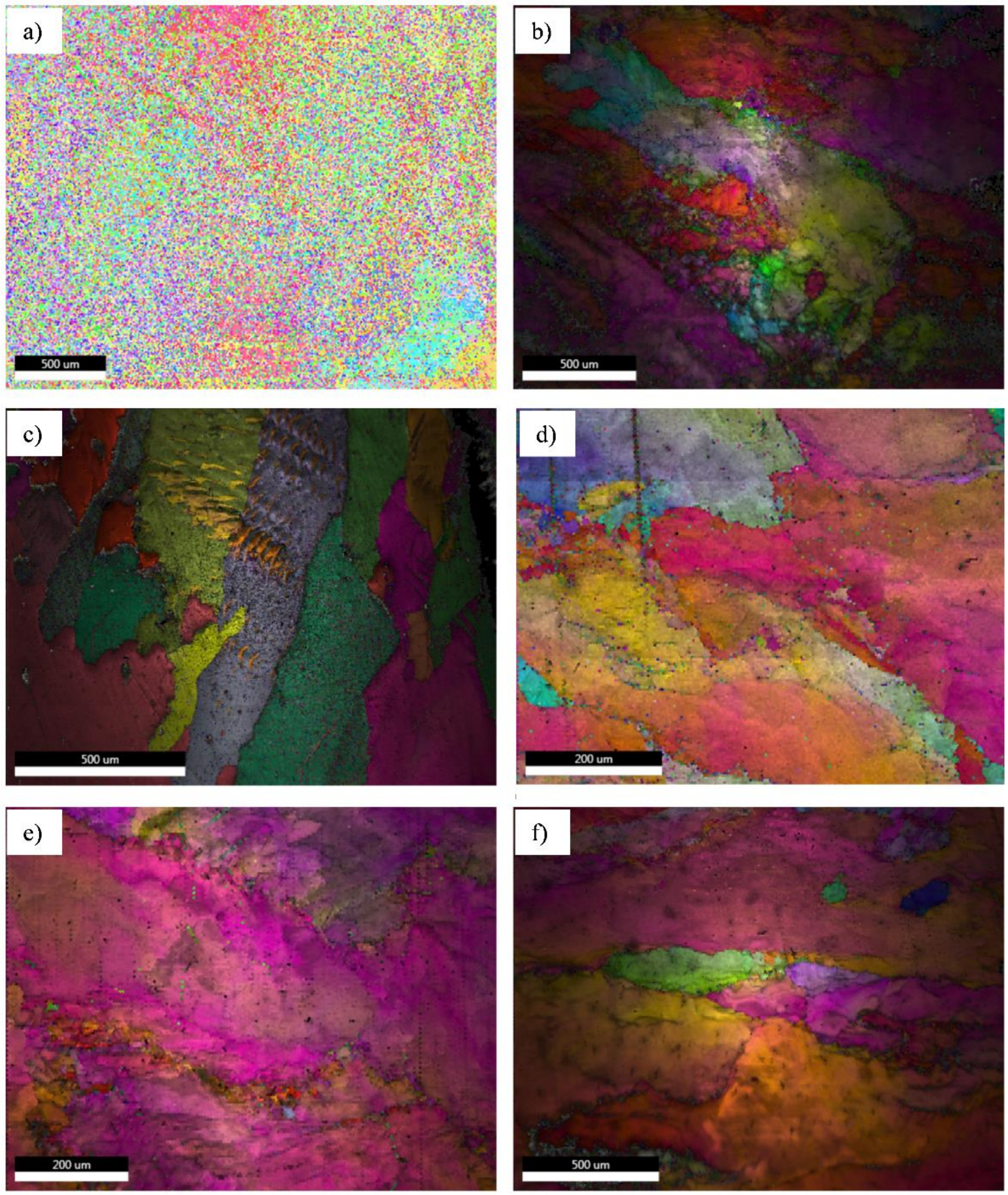

Figure 3.5. EBSD maps illustrating the effects of various surface preparation methods aimed at achieving a stress-free surface: (a) mechanical polishing with 0.05 diamond size suspension followed by 20 seconds of etching (CI= 0.02), (b) mechanical polishing followed by 5 seconds of etching (CI= 0.44), (c) polishing for 2 hours using a 0.25 μm diamond particle emulsion (CI= 0.29), (d) polishing for 2 hours using a 0.05 μm Silica particle suspension (CI= 0.36), and (e, f) polishing for 2 hours using a 0.05 μm diamond particle suspension (CI= 0.55-0.58).

3.3. Nanoindentation experiments

Nanoindentation experiments were carried out using a Hysitron TI 750 Ubi NanoIndenter . A diamond Berkovich tip with an elastic modulus of 1141 GPa and a Poisson's ratio of 0.07 was employed. The tip radius (R) was measured to be approximately 650 nm by fitting the contact area (A) versus contact depth (h_c) to the tip area function, following the Oliver–Pharr method—which accounts for the effects of a rounded indenter tip [27] . The tip area function is given by:

$$A(hc) = 24.5h_c^2 + C1h_c^1 + C2h_c^{1/2} + C3h_c^{1/4} + \dots\dots + C3h_c^{1/128} \qquad \text{Eq. 3.1}$$

Where C1 through C8 are constant, and in our evaluations where C1 = 2.21×10^3 nm, C2 = 4.76×10^{23} nm, and C3 to C8 were set to zero. Figure 3.5 shows the contact area versus contact depth for the Berkovich tip used in our experiment, based on the applied tip area function.

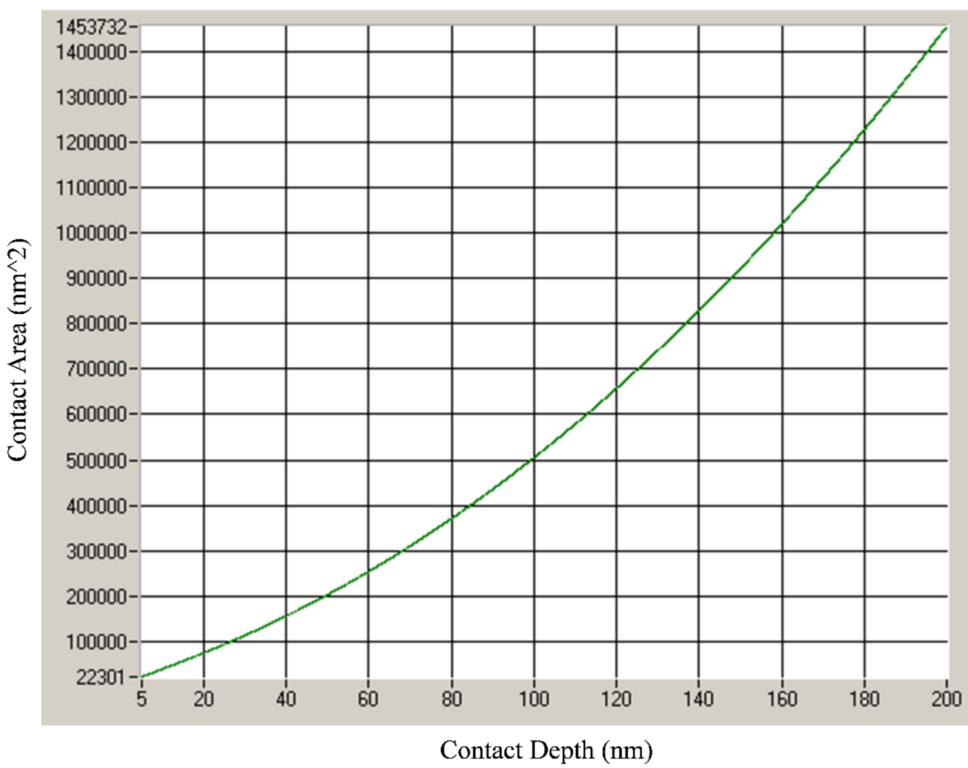

12Figure 3.6. Contact area versus contact depth for the Berkovich tip used in our experiment, derived from the applied tip area function.

To ensure accurate and repeatable results, all nanoindentation tests were conducted under minimal vibration conditions, which involved scheduling experiments only when no other individuals were present in the laboratory to avoid interference from foot traffic. Nanoindentation experiments were carried out under the load-control condition. The loading and unloading segments were conducted at a constant rate, and a short dwell time was applied at the peak load to minimize the effects of creep and thermal drift. Additionally, the sample surfaces were polished to a mirror-like finish, ensuring reliable contact between the tip and the material.

For indentation depth under 0.09R, the material's response resembles that of a spherical indenter with radius R [59]. Given that the first pop-in occurs at a depth of approximately 10-20 nm, the contact mechanics theory for a spherical tip was applied in our study. Figure 3.6 illustrate the apex of the Berkovich indenter tip as observed through scanning electron microscopy.

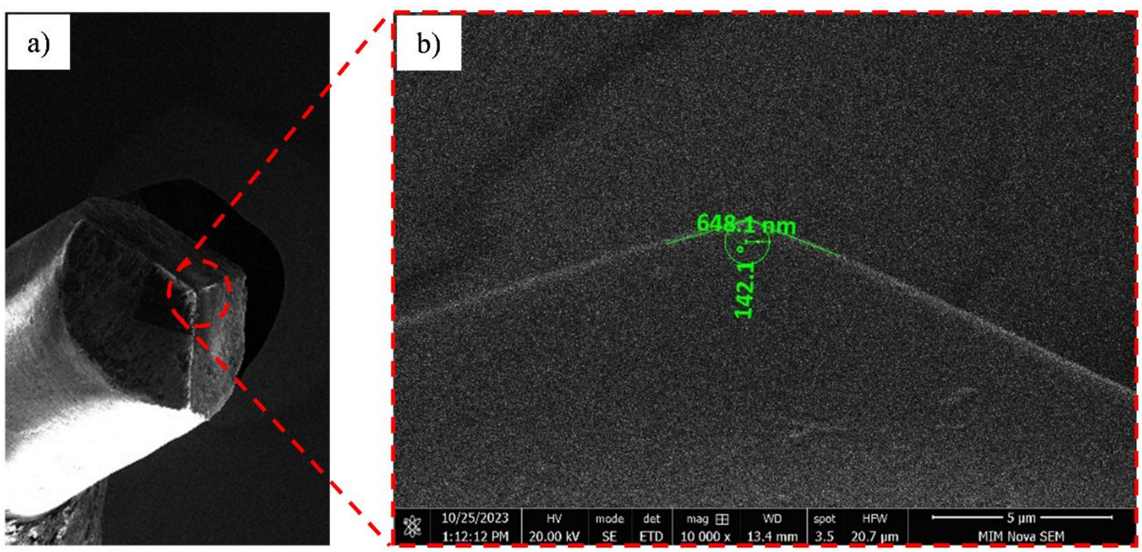

13Figure 3.7. Illustrates the apex of the Berkovich indenter tip as observed through scanning electron microscopy (SEM). a) SEM image of Berkovich tip a) Berkovich tip, b) a top view of the tip.

Because of the stochastic nature of pop-in events during nanoindentation, over 100 indents were made on each grain orientation to ensure sufficient data for statistical evaluation. An interval of 10 µm was maintained between indents to prevent plastic zones or the residual stress from one indent from influencing subsequent measurements. This methodical approach ensures that each indentation event remains independent, providing more reliable insights into the stochastic behavior of pop-in phenomena.

3.3.1. Loading selection

Since the primary objective of this research is to investigate dislocation-based incipient plasticity, the first pop-in event observed in the load-displacement curve serves as a key indicator. To determine the most suitable testing conditions, we evaluated multiple loading scenarios—1000, 2500, 5000, and 12000 μN. A representative load-displacement curve for each is presented in Figure 3. Although all four conditions exhibited pop-in events, the first pop-in was most clearly discernible at 1000 μN. In contrast, the initial pop-in at 2500, 5000, and 12000 μN appeared alongside a substantial deviation—possibly stemming from pre-existing dislocation structures [106, 107]. Only the 1000 μN condition produced a first pop-in closely matching the Hertzian fit, suggesting it is more directly associated with the nucleation of new dislocations rather than the activation of existing defects. This observation is consistent with findings from another experiment reported in the literature [13].

To study dislocation-based incipient plasticity in magnesium (Mg), a low indented volume is needed. Based on the experimental observations under various loading conditions—particularly those that produced a clearer first pop-in—we selected a maximum load of 1000 μN for this study. This load proved optimal for capturing the incipient plasticity processes in Mg, allowing us to more accurately distinguish between dislocation nucleation events and the onset of twinning in our nanoindentation measurements.

Figure 3.7 illustrates various load-displacement (P-h) curves under different loading conditions. In Each curve represents the results of multiple tests conducted under the specified loading conditions.

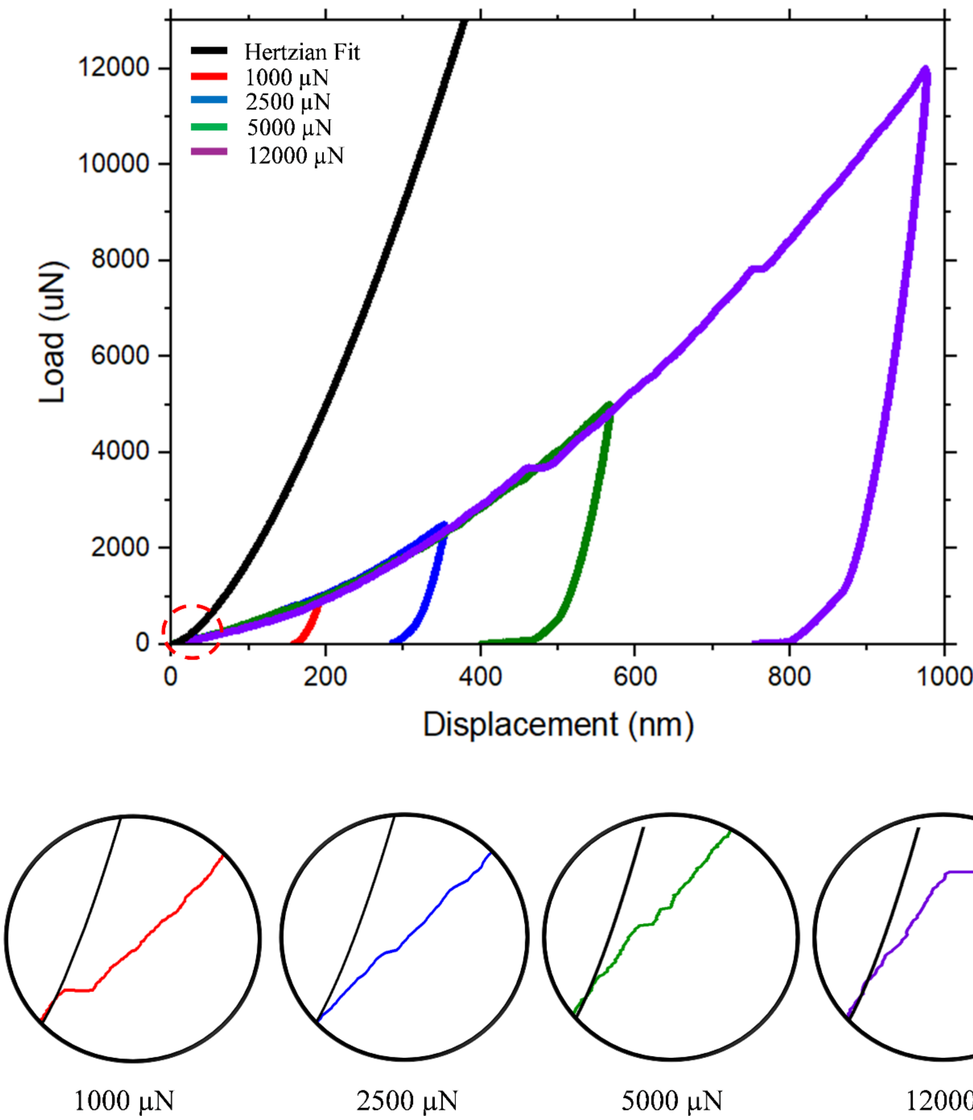

14Figure 3.8. Representative load-displacement (P-h) curves for different loading conditions, illustrating the distinct pop-in events observed under each load level.

3.4. Scanning probe microscopy (SPM)

Scanning Probe Microscopy (SPM) was employed to examine the indentation impressions and any resulting deformation features, such as twinning or slip traces, on the tested surfaces. These observations are crucial for correlating the mechanical response recorded during nanoindentation—such as pop-in behavior or changes in the load-displacement curve—to underlying deformation mechanisms. The SPM analysis was performed using a Hysitron TI 750 Ubi NanoIndenter equipped with a Berkovich tip. By capturing high-resolution topographical data, SPM allows for a detailed investigation of localized plastic deformation, including microcracks or shear bands, that may form around the indent site. Figure 3.8 illustrates the load-displacement (P-h) curve followed by the SPM graph before and after an indentation mark.

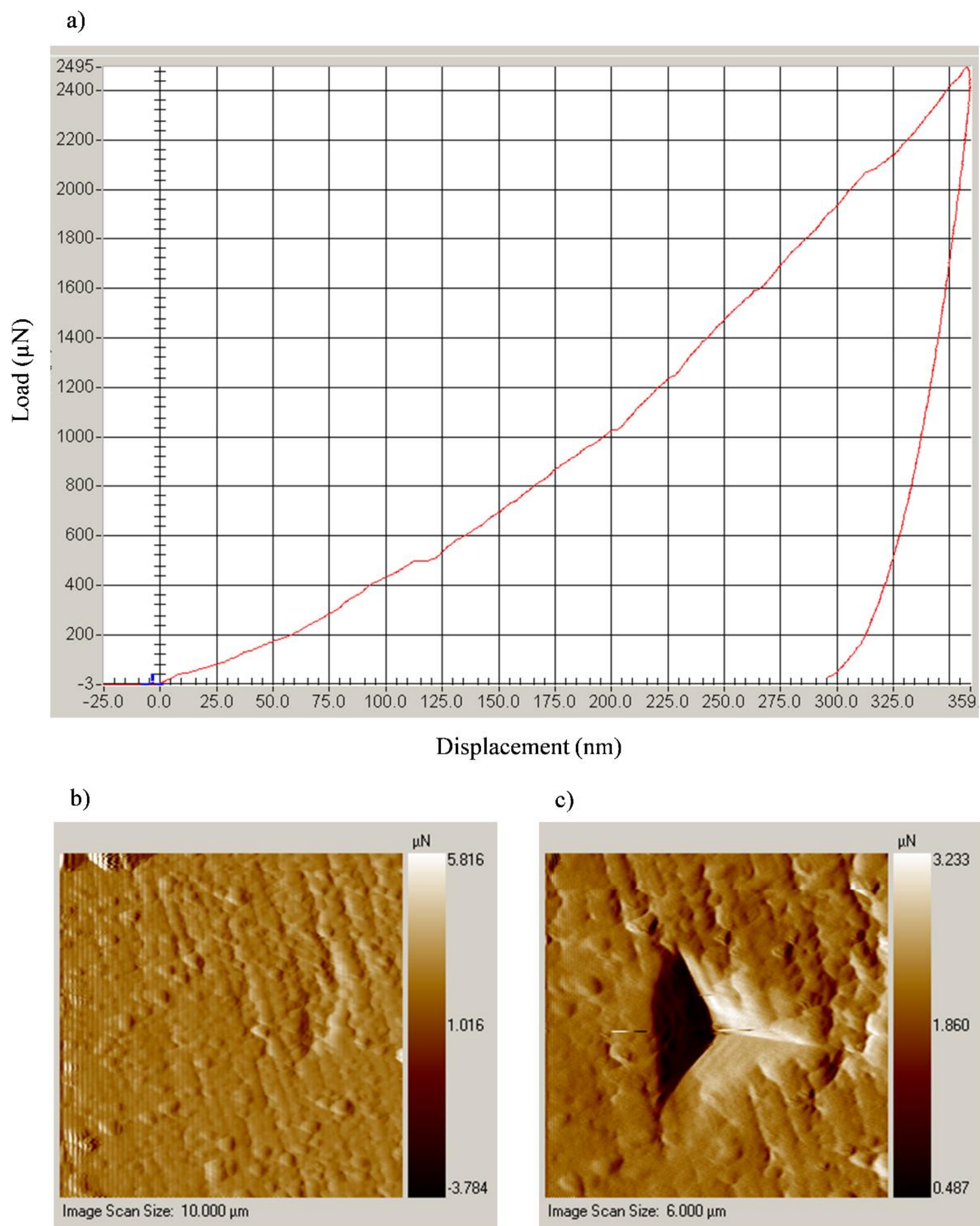

15Figure 3.9. a) Illustration of the load–displacement (P–h) curve, b) SPM graph obtained before indentation, and c) SPM graph obtained after indentation.

3.4.1. Scanning probe microscopy optimization

Since nanoindentation is performed close to the free surface, dislocation activity and twinning propagation can create visible traces around the indentation mark. Slip traces generally appear as linear features[13, 48, 107, 112], while twinning is observed as three-dimensional (3D)-like patterns. Therefore, scanning probe microscopy (SPM) or atomic force microscopy (AFM) analysis can be useful for studying dislocation and twinning activities.

To achieve the highest resolution in SPM imaging for our experiments, we optimized various scanning parameters. SPM imaging resolution is influenced by five key parameters: scan rate (SR), step point (SP), integral gain (IG), scan size (SS), and tip velocity (TV). These parameters are defined as follows:

Scan Rate (SR): The speed at which the probe moves across the sample surface, typically measured in lines per second (Hz).

Step Point (SP): The force applied by the nanoindentation probe while in contact and in feedback with the sample surface. The default value is 2.0 μN.

Integral Gain (IG): The sensitivity of the system to signals generated by the tip's motion.

Tip Velocity (TV): The speed at which the probe moves over the sample surface, dependent on the scan rate and scan size, affecting image quality.

For optimization, we kept the tip velocity and scan size constant, while adjusting the remaining parameters to achieve the highest resolution for nanoindentation imaging at 1000 μN load. The optimization trials and their corresponding results are summarized in Table 3.1.

In Trial 1, we used the default values SR = 1, SP = 1, and IG = 240, which resulted in poor image resolution of the indentation mark and surrounding area. In Trials 2 and 3, we increased SP to 2 and 5, respectively, while maintaining the same conditions as in Trial 1. This adjustment significantly improved the resolution. In Trial 4, we increased IG without changing other parameters compared to Trial 1, but this did not yield satisfactory results. In Trial 5, we simultaneously increased both SP and IG, which produced the highest resolution images.

Additionally, in Trials 7 and 8, we tested lower and higher values of SR compared to the default value SR = 1. However, the best resolution was achieved with SR = 1.

Based on our optimization study, the optimal parameters were identified as either SR = 1, SP = 2, IG = 500 (Trial 5) or SR = 1, SP = 5, IG = 240 (Trial 3). Since a higher IG was more sensitive to external noise, such as vibrations caused by movement in the laboratory, we selected Trial 3 (SR = 1, SP = 5, IG = 240) as the optimized condition for subsequent tests.

Table 3.1. Overview of SPM results under various experimental conditions, highlighting the key parameters and corresponding surface observations.

Iteration	SR	SP	IG	Result	Explanation
Trial 1 – Default values	1	1	240	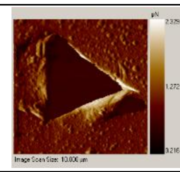	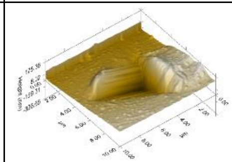
Trial 2	1	2	240	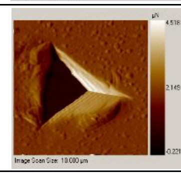	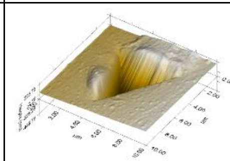
Trial 3	1	5	240	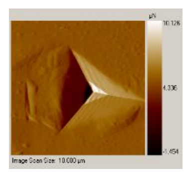	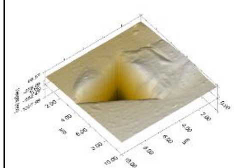
Trial 4	1	1	500	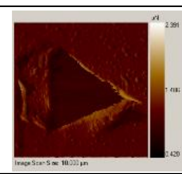	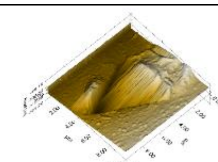
Trial 5	1	2	500	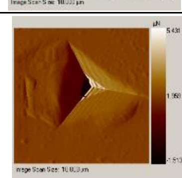	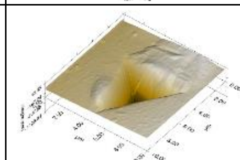
Trial 6	1	5	500	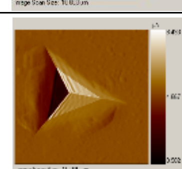	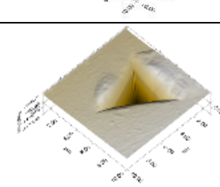
Trial 7	0.5	2	500	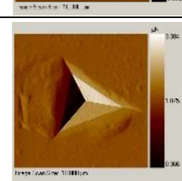	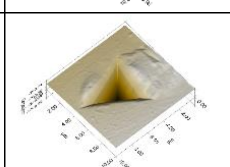
Trial 8	2	2	500	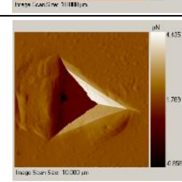	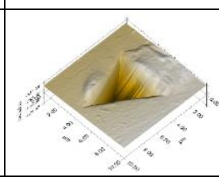

3.5. Possibility of Twinning nucleation/activation

As it mentioned earlier, under nanoindentation, both dislocation slip and mechanical twinning can be nucleated and activated. When these defects extend to the material's surface, they typically leave characteristic traces.

In our study, the potential for twin nucleation and its corresponding surface traces around the nanoindentation sites were investigated with SPM and High-resolution SEM (HRSEM) for five different grain orientations (O1–O5), as illustrated in Figure 3.9.

Furthermore, the twin variant plane and direction exhibiting the highest indentation Schmid factor were identified using Vesta software to predict the most likely trace. To facilitate this prediction, the atomic structure was projected along the normal to the chosen orientation plane, thereby providing a clear visualization of the anticipated twin plane and direction. Table 3.2 presents the grain orientations along with their corresponding Euler angles, grain planes, normal directions, and the most likely extension and compression twin planes and directions. In table 3.3, P-h curve, pre- and post-nanoindentation SPM images, HRSEM results, and the simulated most probable extension/contraction twin planes and directions are listed.

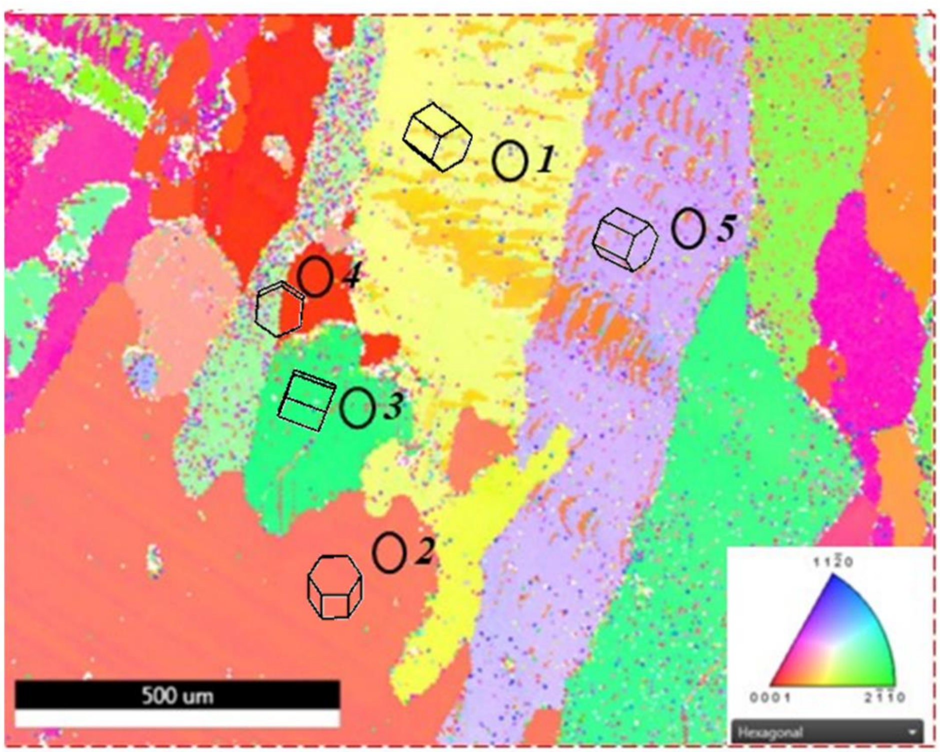

16Figure 3.10. EBSD map illustrating five distinct grain orientations (O1–O5).

Table 3.2. listed the Euler angles, plane and normal direction, and the highest possible extension and compression twin in each grain orientation.

Grains	**Euler angle (ϕ, θ, ψ)**	**Grain Plane**	**Load direction (Normal to plane)**	**Extension twin system**	**Compression twin system**
O1	142.7, 126.2, 334.3	(-4 9 -5 -10)	[-24 11 13 13]	(-1 2 -1 1) [1 -2 1 6]	(-1 1 0 1) [-1 1 0 -2]
O2	147.4, 25.8, 14.1	(1 0 -1 -3)	[-3 0 3 -2]	(1 1 -2 1) [-1-1 2 6]	(1 1 -2 2) [1 1 -2 -3]
O3	339.5, 91.3, 279	(-27 17 10 -1)	[1 5 -6 -2]	(1 -1 0 2) [-1 1 0 1]	(2 -1 -1 2) [2 -1 -1 -3]
O4	82.02, 173.2, 27.8	(1 1 -2 -27)	[21 15 -36 4]	(0 1 -1 2) [0 -1 1 1]	(-1 -1 2 2) [-1 -1 2 -3]
O5	333.7, 62.2, 252.8	(-23 5 18 20)	[-4 8 -4 -3]	(-1 0 1 2) [1 0 -1 1]	(1 0 -1 1) [1 0 -1 -2]

Table 3.3. P-h curve, pre- and post-nanoindentation SPM images, HRSEM results, and the simulated most probable extension/contraction twin planes and directions

Grain	P-h curve	SPM before test	SPM after test	HRSEM after test	Extension twin system	Compession twin system
O1	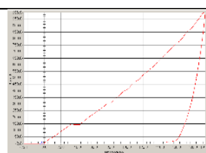	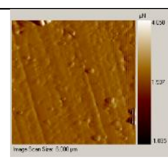	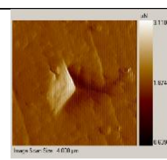	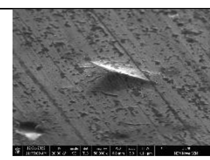	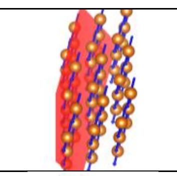	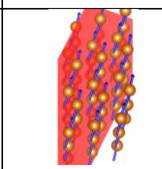
O2	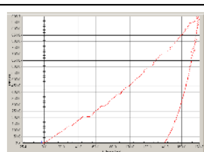	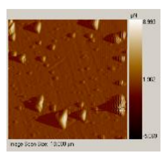	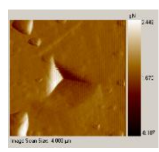	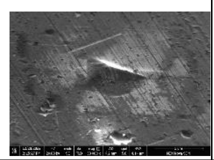	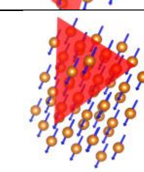	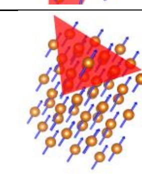
O3	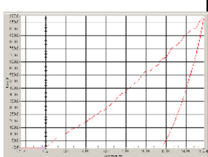	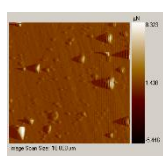	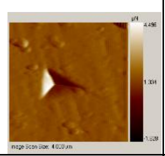		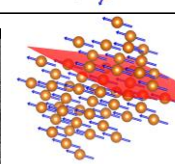	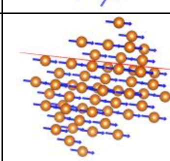
O4	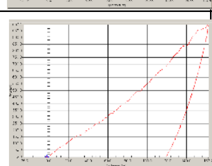	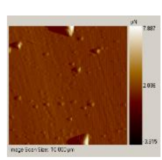	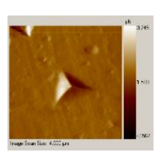		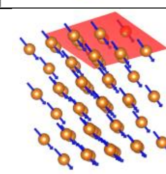	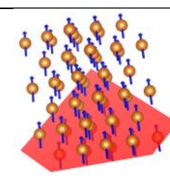
O5	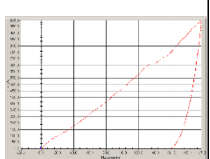	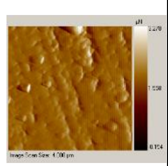	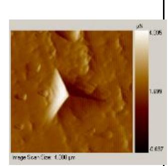	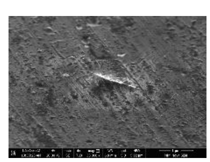	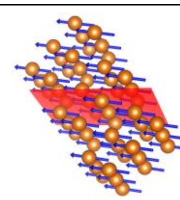	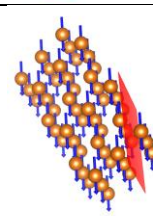

Analyses revealed no visible twin traces around the nanoindentation imprint, suggesting a low probability of twinning at the applied load conditions. Although twinning may still occur at subsurface levels, a lack of visible surface traces indicates reduced likelihood of twinning under these specific conditions, consistent with previous reports [10, 13]. In all grain orientations, some linear features—mostly visible in the HRSEM images—are observed. These lines, which share the same direction across different regions, are most likely polishing-induced scratches rather than slip traces. This conclusion is further supported by a comparison with SPM images taken prior to indentation, where the same lines are already present, confirming their origin as surface preparation artifacts.

3.6. Grain location Identification

Initially, an area of interest was marked on the sample (Figure 3.10 (a)), and then a 2.5 × 1.5 mm EBSD map was created (Figure 3.10 (a)) to encompass various grain orientations. To ensure precise identification of test locations, large load indentations of 12000 μN were made to sign the area, as depicted in Figure 3.10 (c). This signed area was then re-checked using another EBSD map to confirm the target locations (Figure 3.10 (d)). Subsequently, a directional map was generated to identify different grain orientations, as shown in Figure 4(b), which illustrates the directions and distances from the marked Grain 1 (G1) area to neighboring grain orientations. This procedure, involving signing with 12000 μN indentations and verification with EBSD, was meticulously repeated for each grain orientation. Figure 4 presents the flowcharts, the marked area, the EBSD map, the optical microscope image of the designated area in Grain 1 (G1), and the schematic of nanoindentation on selected grain orientations.

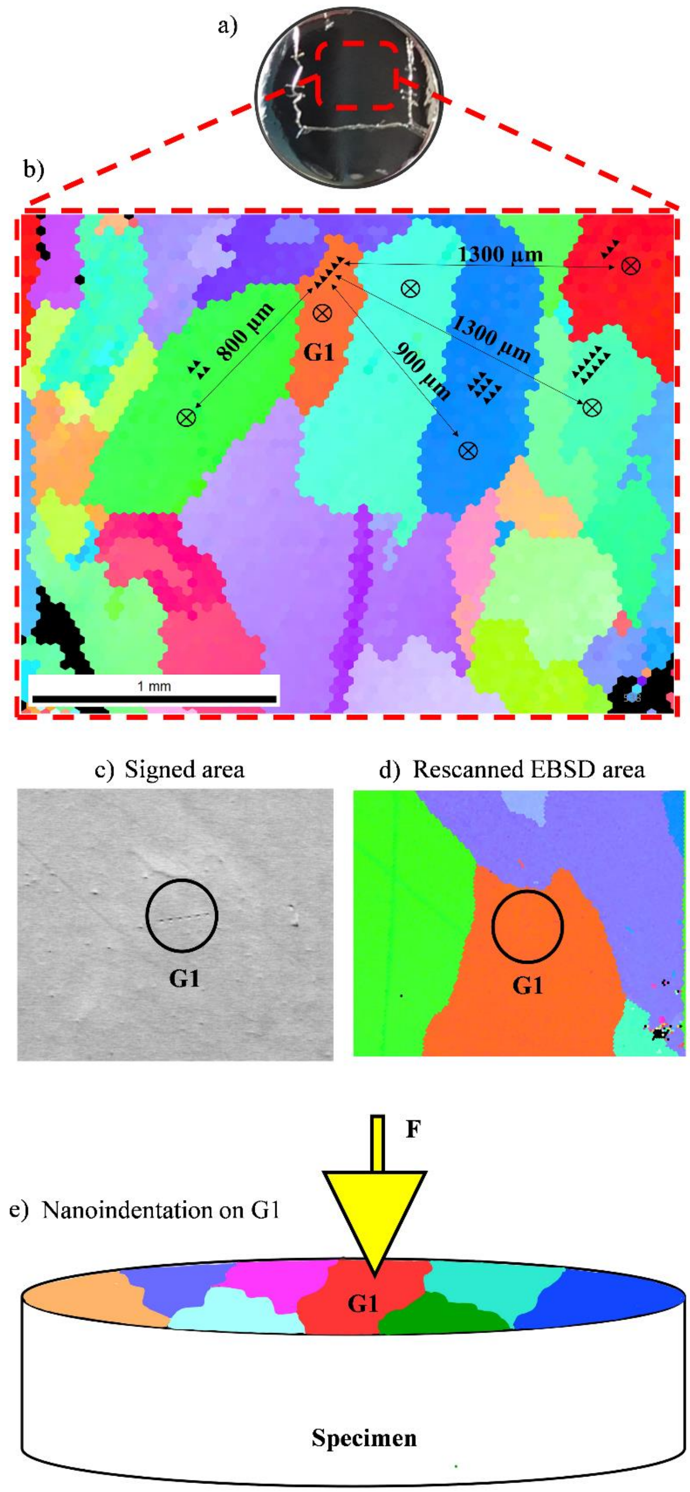

Figure 3.11. Grain location identification. (a) Sample with marked area, (b) directional EBSD map for locating different grain orientations, (c) optical microscope image of the designated area in (G1) with 12000 μN load, (d) EBSD map of the designated area in G1 for checking the indented location, and e) Schematic graph of nanoindentation experiments on one selected grain orientation

3.7. Grain Orientation Coverage

In order to capture different grain orientations , different grain orientations were identified through the EBSD analysis, which is illustrated in Figure 3.12 (a-e). Using a grain-signing-finding approach, thirteen distinct orientations were selected—labeled G1 through G13—for the nanoindentation experiments. Figure 3.12 (f) shows an inverse pole figure (IPF) image of these orientations, illustrating the diversity of the selected grains.

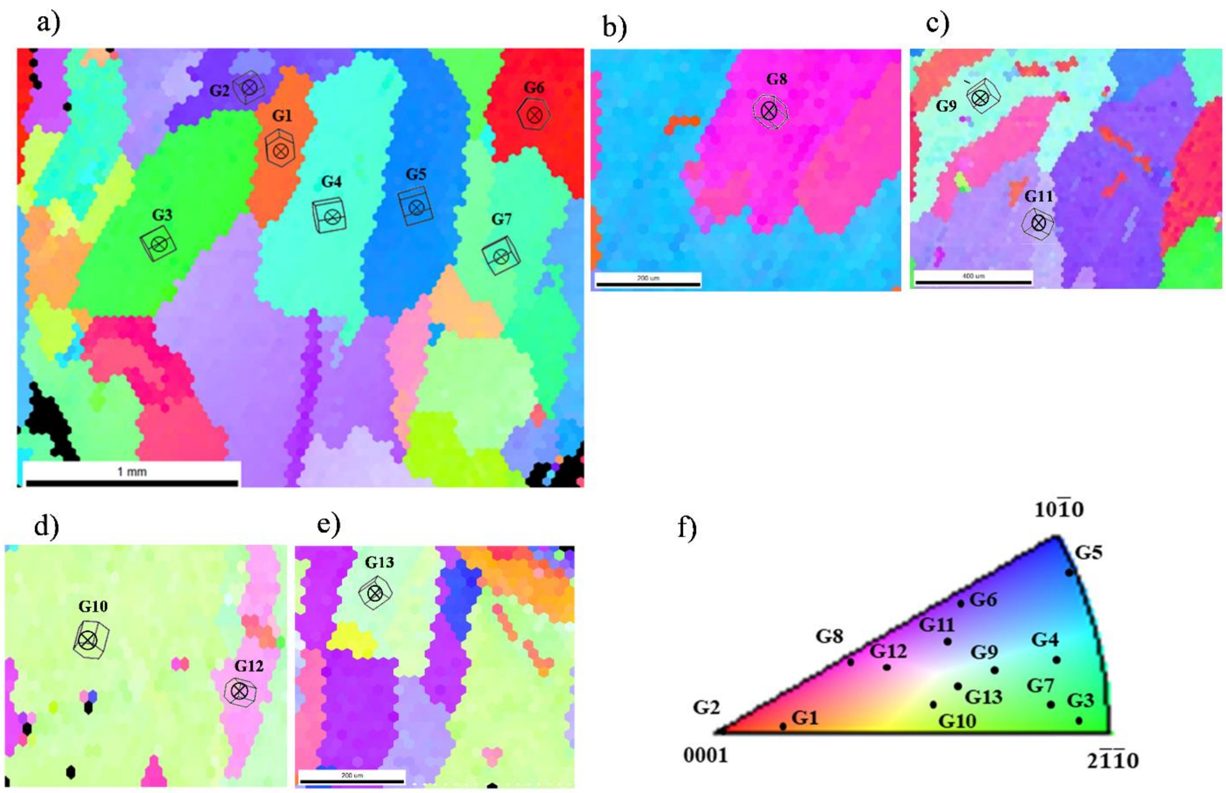

17Figure 3.12. Selection of thirteen distinct grain orientations, labeled G1 through G13 in the IPF image.

3.8. Pop-in evaluation

In our experiments, multiple elastic-to-plastic transition behaviors were observed, as illustrated in Figure 3.12. A limited number of curves exhibited load–displacement (P–h) responses that deviated significantly from the Hertzian fit, showing complete divergence from the expected trend. Such behavior could be attributed to several factors, including the presence of pre-existing dislocations or surface discontinuities such as scratches. Regardless of the underlying cause, these cases were excluded from our statistical analysis, as the focus of this study is on dislocation nucleation. Figure 3.12 (a,b) shows instances of such divergent curve, characterized by significant anomalies in the load–displacement curves. In contrast, Figure 3.12 (c,d) illustrates the classic "ideal" pop-in response, marked by a sudden and distinct displacement burst indicating the onset of plasticity. Meanwhile, Figure 3.12 (e,f) captures an excursion occurring just before the pop-in event, and Figure 3.12 (g,h) demonstrates a deviation in the load–displacement curve immediately prior to pop-in. All these distinct behaviors were documented in the G1 dataset, although similar transitions from elastic to plastic were observed in other crystallographic orientations as well.

Because these incipient plasticity phenomena occur at very low displacement and load levels, a precise understanding of the noise level and well-defined detection criteria are essential. Such measures help to reliably separate genuine material responses from instrumental or environmental noise, thereby ensuring reproducible measurements and deeper insight into the underlying deformation mechanisms.

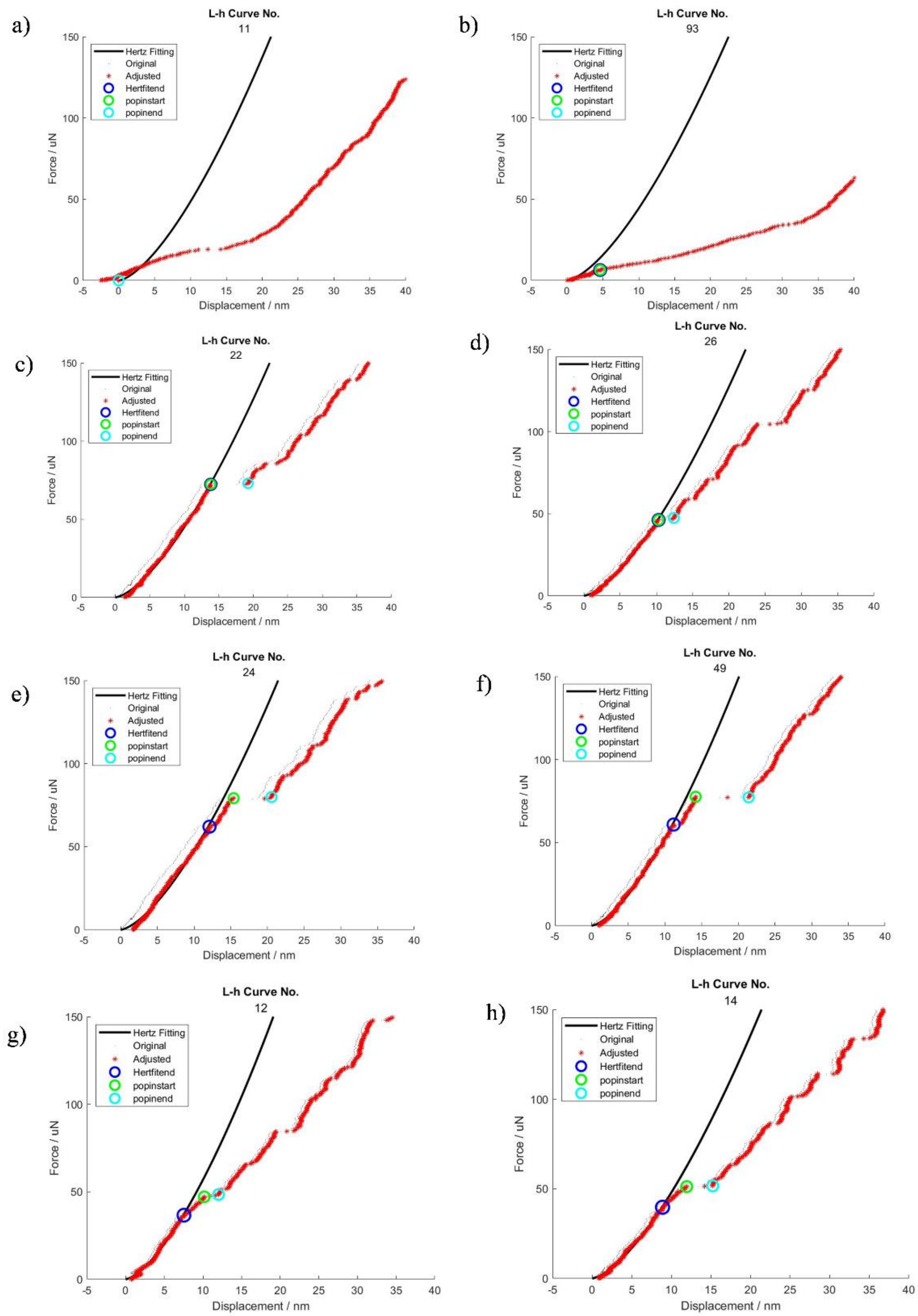

18Figure 3.13. Various elastic-to-plastic transition behaviors in the load–displacement (p–h) curve: (a, b) Divergent cases; (c, d) ideal pop-in; (e, f) excursions preceding pop-in; (g, h) deviations just before pop-in.

3.8.1 Experimental Noise Evaluation

The first pop-in event, observed as a sudden displacement burst in the load–displacement (P–h) curve, typically signifies the onset of plastic deformation. However, if there are fluctuations in the load-displacement (P–h) curve caused by surface scratches or discontinuities, they may be indistinguishable from true incipient plasticity events [27], potentially introducing errors into the data . Therefore, analyzing the instrument's noise level under our experimental conditions is essential. To quantify the experimental noise, the differences between the experimentally measured displacement (d_E) and the predicted displacement using the Hertzian fit (d_H) are calculated for >10 randomly selected p-h curves for G1. The Hertzian fit covers the entire elastic deformation region up to the onset of either the excursion or the first pop-in. As shown in Figure 3.13, the deviation ($d_E - d_H$) generally follows the normal distribution, with a standard deviation (σ) of approximately 0.2 nm. Thus, the displacement burst higher than FWHM of 0.46 nm can be considered as the materials' response.

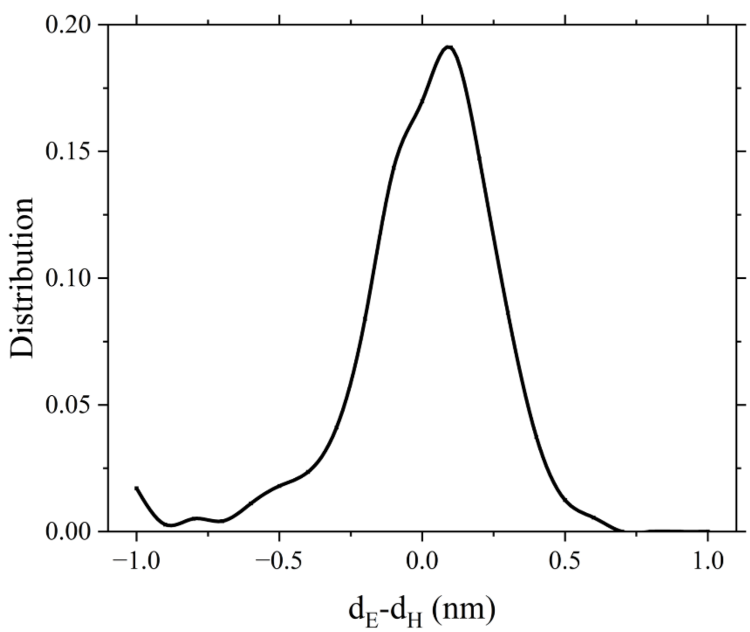

19Figure 3.14. The distribution of displacement noise (dE−dH) with an FWHM of ~0.46 nm, indicates the instrument's noise level.

3.8.2 Pop-in criteria

Based on the nanoindentation results (Figure 3.12), any experiment that did not closely follow the Hertzian contact model was deemed invalid and excluded from further analysis. Since the first pop-in event corresponds to incipient plasticity, a distinct change in the load–load-displacement slope immediately afterward confirms the onset of plastic deformation. Accordingly, detecting such a slope change provides a clear criterion for validating the presence of a pop-in.

In contrast, excursions typically involve smaller displacement magnitudes (less than 1 nm) compared to pop-ins, and the loading curves remain well aligned with the Hertzian slope after these minor bursts. The statistical distribution of displacement bursts arising from excursions and pop-ins (Figure 3.14) shows that the average excursion length is approximately 0.76 nm, whereas the average first pop-in length is substantially larger, at about 5.1 nm. This clear difference highlights the distinct nature of excursions versus pop-ins. Moreover, since the average excursion length exceeds three times the standard deviation of the noise level, we conclude that these excursions also represent a genuine manifestation of incipient plasticity.

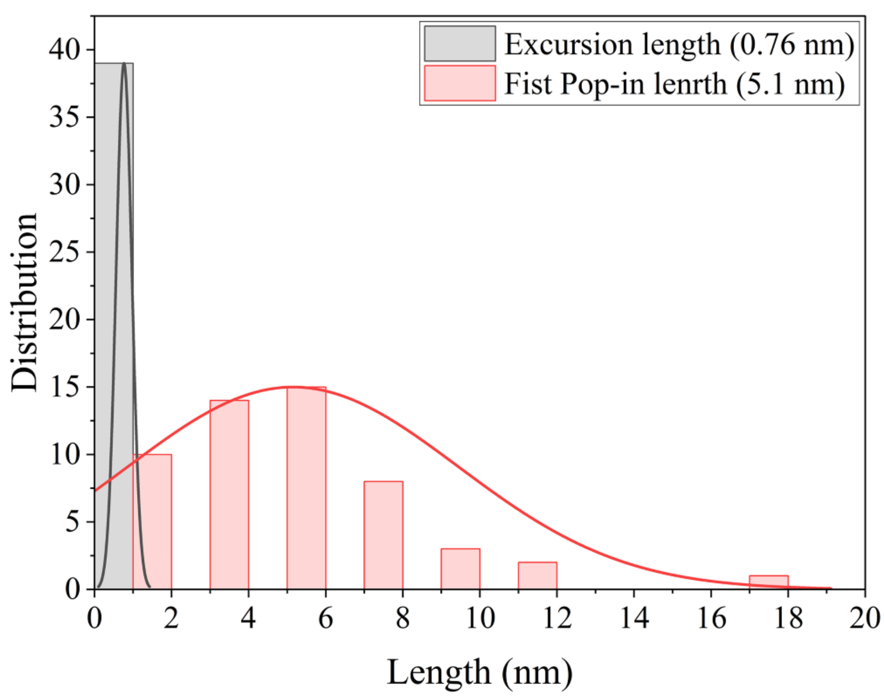

20Figure 3.15. Distribution of excursion and first pop-in lengths for G1. The average excursion length (gray distribution) is 0.76 nm, while the average first pop-in length (red distribution) is 5.1 nm.

Based on the aforementioned discussion, we established the following criteria for detecting the first pop-in event:

a) acceptable hertzian fit in initiation of curve,

b) pop-in length > 1 nm,

c) different curve slope after the 1st pop-in compared to the hertzian fit.

Based on the above-mentioned criteria, the first pop-in characteristics were analyzed using MATLAB software in combination with the PopIn MATLAB toolbox. To ensure accuracy and consistency across all grain orientations, three critical points were carefully identified for each load-displacement (P-h) curve: the Hertz endpoint (defining the end of the purely elastic region), the start of the pop-in, and the end of the pop-in. Figure 3.15 illustrates a representative analyzed p-h curve as an example.

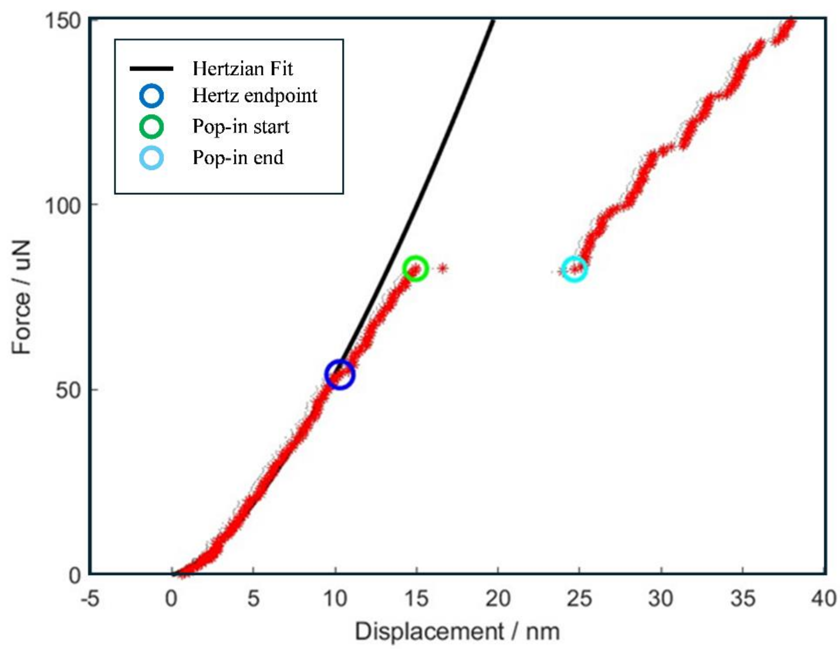

21Figure 3.16. Actual load-displacement curve with identified Hertz endpoint, the Pop-in start, and the Pop-in endpoint.

3.9. Conclusion

In this chapter, the materials and methodologies employed in this research were discussed in detail, emphasizing the experimental design aimed at investigating dislocation-based incipient plasticity in nanoindentation while excluding twinning. Particular attention was given to covering various grain orientations to ensure a comprehensive evaluation. The key procedure can be summarized as follows:

1. A stress-free surface of Mg-Gd alloys was successfully prepared using only mechanical polishing with a 0.05 μm polycrystalline diamond glycol-based suspension. This etch-free procedure yielded a high confidence index for EBSD analyses and provided a mirror-like finish suitable for nanoindentation measurements, eliminating the need for chemical etching commonly reported in the literature.
2. The nanoindentation conditions for studying dislocation-based incipient plasticity were optimized using a 1000 μN load, which resulted in more clearly observable pop-in events occurring at low loads (<100 μN) and shallow displacements (approximately 10–20 nm). These conditions produced a small indented volume, making them suitable for minimizing the likelihood of twinning nucleation. By applying a precise "grain signing-finding approach," nanoindentation experiments were conducted on 13 different grain orientations, with over 100 indents per orientation.
3. The instrument's noise level was estimated by analyzing the distribution of displacement noise, which exhibited a full width at half maximum (FWHM) of approximately 0.46 nm. This indicates that displacement bursts exceeding this threshold can be considered indicative of incipient plasticity rather than experimental artifacts.

Chapter 4 – Orientation dependence of incipient plasticity

4.1. load-displacement (p-h) curves and first pop-in categories

Upon examining the load-displacement (p-h) curves for all individual grains, we identify three distinct categories of the initial pop-in events, as illustrated in Figures 4.1 to 4.3 for selected grains. These categories are defined as follows:

i) Ideal first pop-in: Pop-in occurs immediately after the Hertzian fit

ii) First pop-in with deviation: The first pop-in occurs following a slight deviation (<5 nm) in the slope from the Hertzian fit

iii) First pop-in with excursion: The first pop-in occurs after a minor excursion (<1 nm) from the Hertzian fit. After the excursion, the load-displacement curve can still be well predicted by the Hertzian fit, accounting for the additional displacement caused by the excursion. This suggests that only elastic deformation occurs between the excursion and the first pop-in.

The criterion of <1 nm for the excursion is determined based on the statistical distribution of displacement bursts induced by either excursions or pop-ins. G1 is selected to demonstrate the typical length distribution of displacement bursts, as shown in Figure 3.14.

In addition to the initial pop-in event, we identified two distinct pop-in behaviours, including single pop-ins (illustrated in Figures 4.2, and 4.3) and successive pop-ins (Figure 4.1). Single pop-in events typically present as a single abrupt displacement burst. After the single pop-in, the slope of the curve changes, which suggests the plastic deformation regime. In contrast, successive pop-ins involve multiple abrupt displacements within the same load-displacement curve slope between each pop-in. By examining both types, we gain deeper insight into the underlying mechanisms governing incipient plasticity, including variations in dislocation nucleation and slip processes.

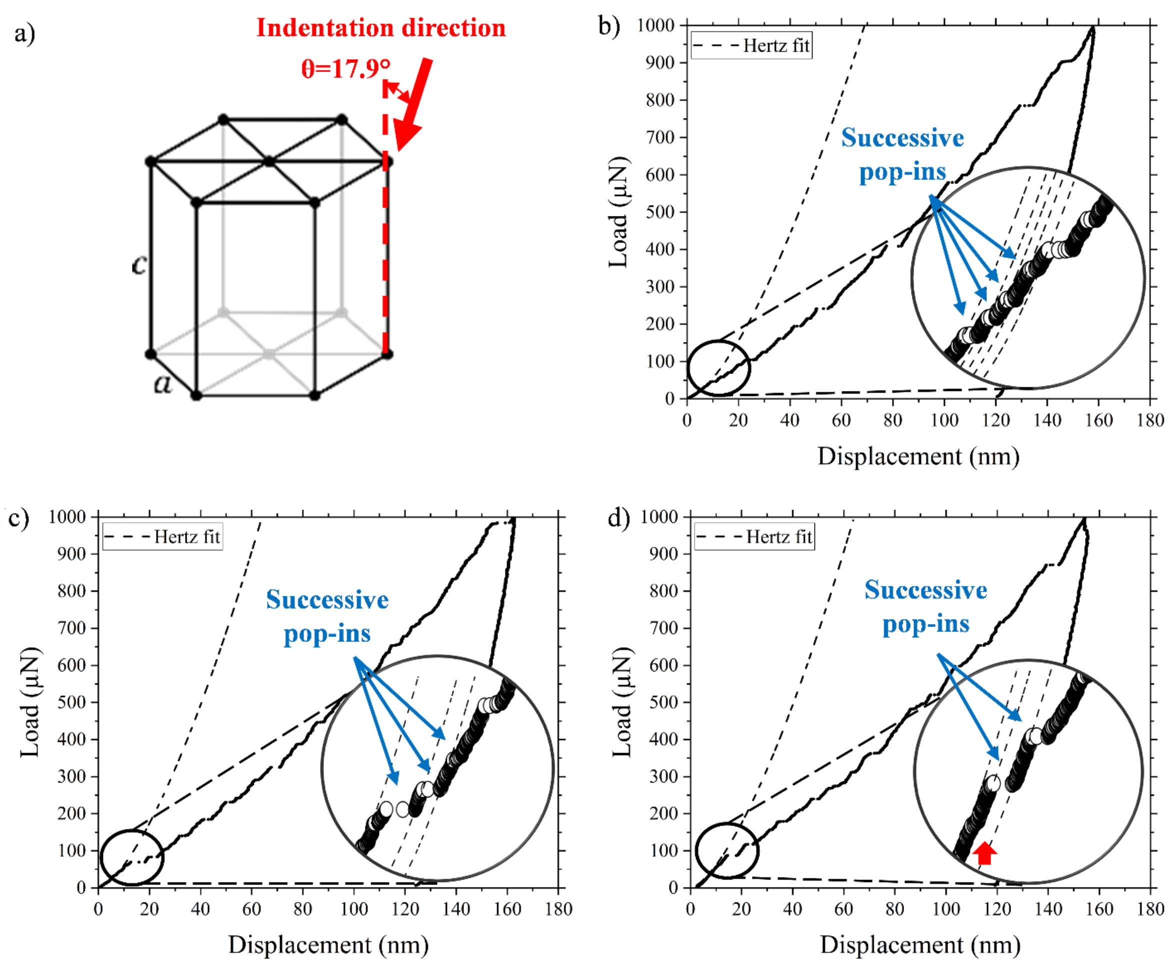

Figure 4.1. Selected load-displacement curves in G1. a) G1: the applied loading direction is 17.9 ° off the c-axis, b) Ideal first pop-in state (21% curves), c) deviation before first pop-ins (29% curves), d) Excursion before first pop-ins (51% curves). The red arrow indicates the slight excursion before the first pop-in, and the blue arrows determine other pop-ins.

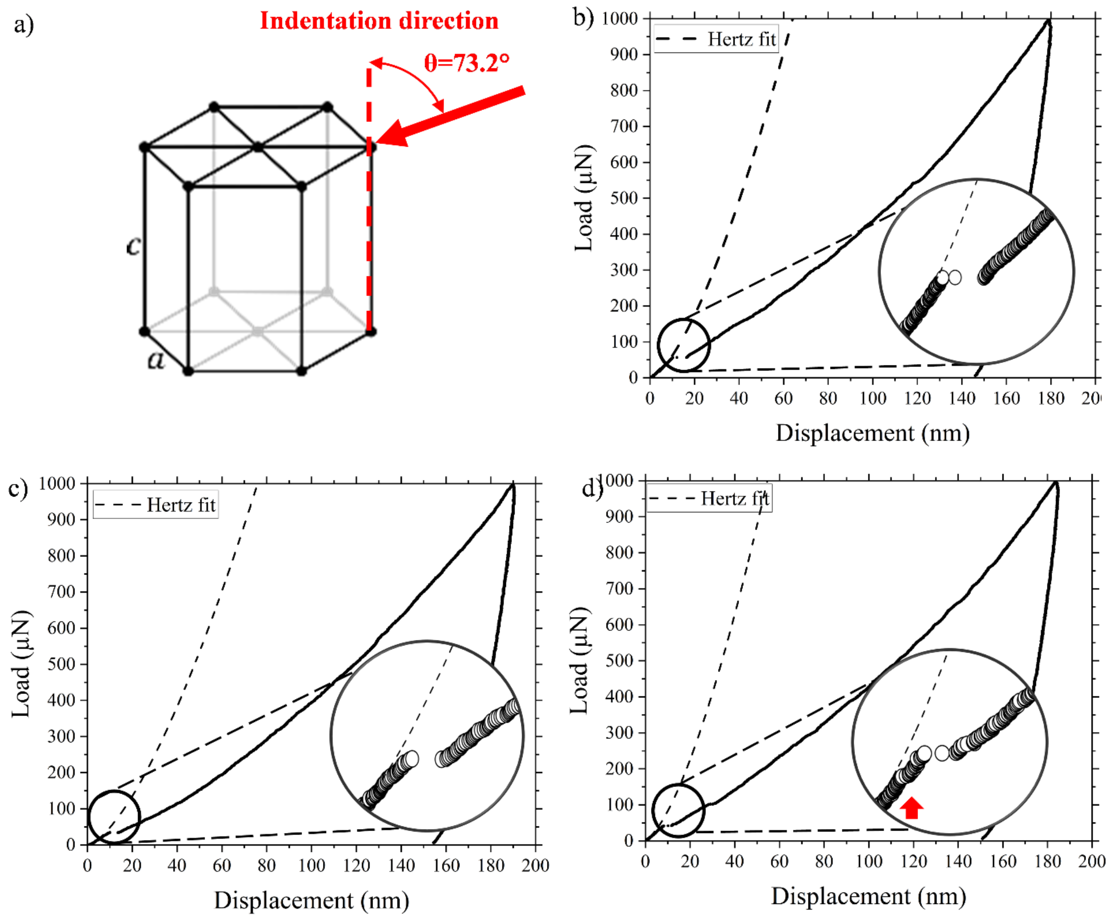

Figure 4.2. Selected load-displacement curve in G6. a) G6: the applied loading direction is 73.2° off the c-axis, b) Ideal first pop-in state (35% curves), c) deviation before first pop-ins (58% curves), d) Excursion before first pop-ins (7% curves). The red arrow indicates the slight excursion before the first pop-in.

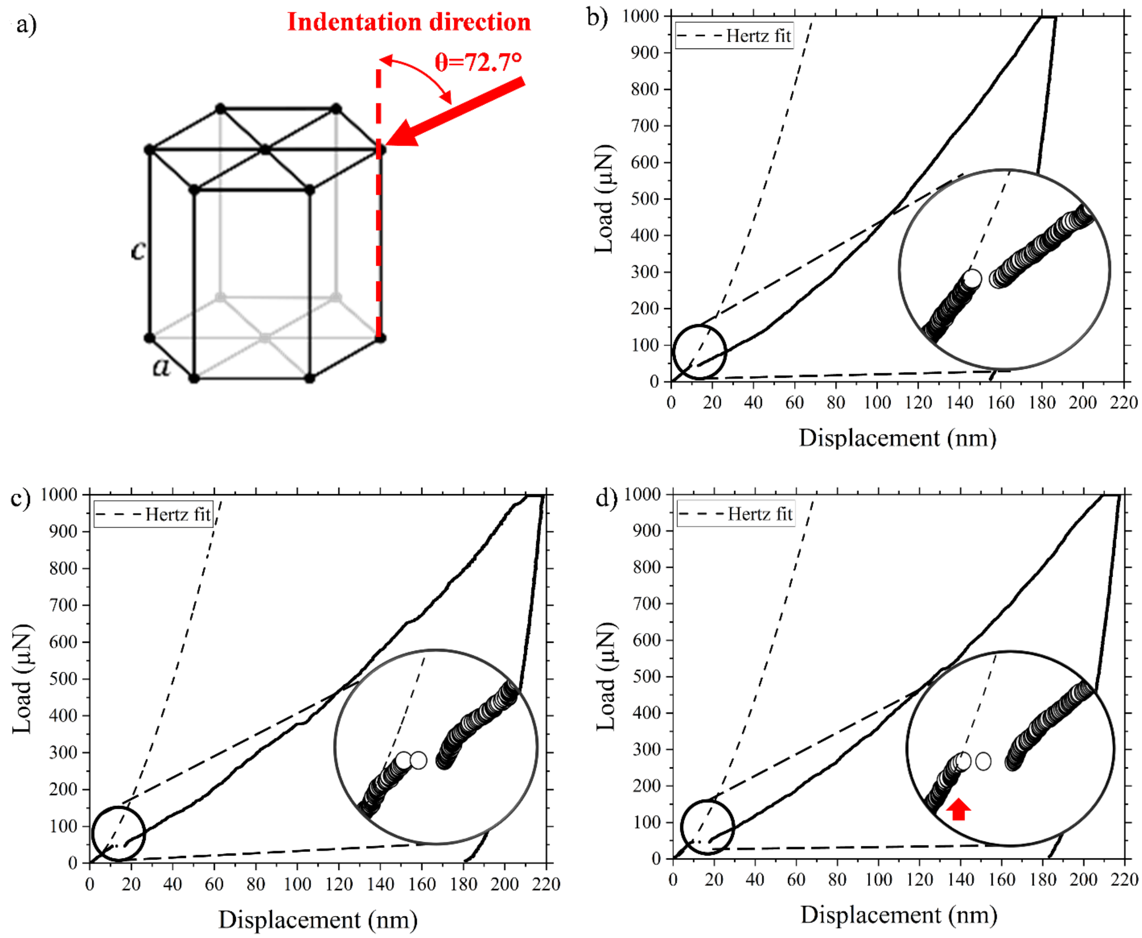

Figure 4.3. Selected load-displacement curve in G9. a) G9: applied loading direction is 83.7° off the c-axis, b) Ideal first pop-in state (36% curves), c) deviation before first pop-ins (60% curves), d) Excursion before first pop-ins (4% curves). The red arrow indicates the slight excursion before the first pop-in.

4.2. Orientation-dependence of p-h curves

4.2.1. Pop-in initiation and pop-in modes

As mentioned earlier, the initiation of pop-in was observed in three categories. All grains exhibited these three types of pop-in modes, albeit with varying frequencies. The orientation dependence of the p-h curve is evaluated by statistical evaluation though all p-h curves for each grain orientation, which is summarised in Table 4.1.

G1 and G2, whose loading directions are nearly perpendicular to the basal plane, exhibit approximately 50% of their p-h curves showing excursions prior to the first pop-in event.

Moreover, successive pop-ins, including excursions, first pop-ins, and a few subsequent pop-ins, are frequently detected in these two orientations; however, such occurrences are rarely observed in the other grains. Grains G3-G13 exhibit deviations prior to the first pop-in, as observed in over ~50% of the load-displacement (p-h) curves, except for grain G5, which displays an ideal pop-in in 68% of the cases. Table 1 lists the loading direction relative to the c-axis (θ°) for each grain orientation, along with the median pop-in load for each grain orientation.

Table 4.1. The percentage distribution of each type of initial pop-in event across various grain orientations, along with the loading direction relative to the c-axis (θ°) and the median pop-in load for each orientation.

Grain	**Euler angles (ϕ, θ, ψ)**	**loading directions relative to the c-axis (θ°)**	**Median pop-in Load (μN)**	**Ideal first pop-in (%)**	**Deviation before first pop-in (%)**	**Excursion before first pop-in (%)**
G1	99.7, 162.1, 275.4	17.9	66.5	20	29	51
G2	344.1, 1.8, 99.1	1.8	69.7	41	13	46
G3	27.7, 94.8, 91.5	85.2	49.7	40	49	6
G4	190.1, 83.7, 196.7	83.7	47.1	36	60	4
G5	195.9, 89.9, 6.7	89.9	44.7	65	28	7
G6	208.8, 73.2, 182.1	73.2	51.0	35	58	7
G7	206.7, 97.9,205.6	82.1	57.6	17	78	5
G8	139.2, 44.3, 358.7	44.3	47.2	16	72	12
G9	35.4, 72.7, 283.4	72.7	44.9	38	51	11
G10	154.4, 65.2, 9.7	65.2	40.6	38	52	10
G11	255.1, 60.1, 260.5	60.1	43.2	21	65	14
G12	165.2, 52.1, 8.8	52.1	49.9	25	64	11
G13	35.5, 65.8, 281.9	65.8	46.4	20	69	11

4.2.2. First pop-in load

Pop-in load distributions for selected grains (G1, G6, and G9) are shown in Figure 4.4. Each grain orientation exhibits a relatively broad range of pop-in loads, with a standard deviation of approximately 20 µN. This variability may arise from minor surface defects, microstructural inhomogeneities, variations in crystal quality [64, 114], or the activation of multiple dislocation mechanisms during the early stages of plasticity, all of which can contribute to the observed spread in pop-in loads [65]. The median pop-in load for each grain orientation is summarized in Table 4.1. It can be observed that grains G1 and G2 display notably higher pop-in loads in comparison to the other orientations, emphasizing the strong crystallographic dependence.

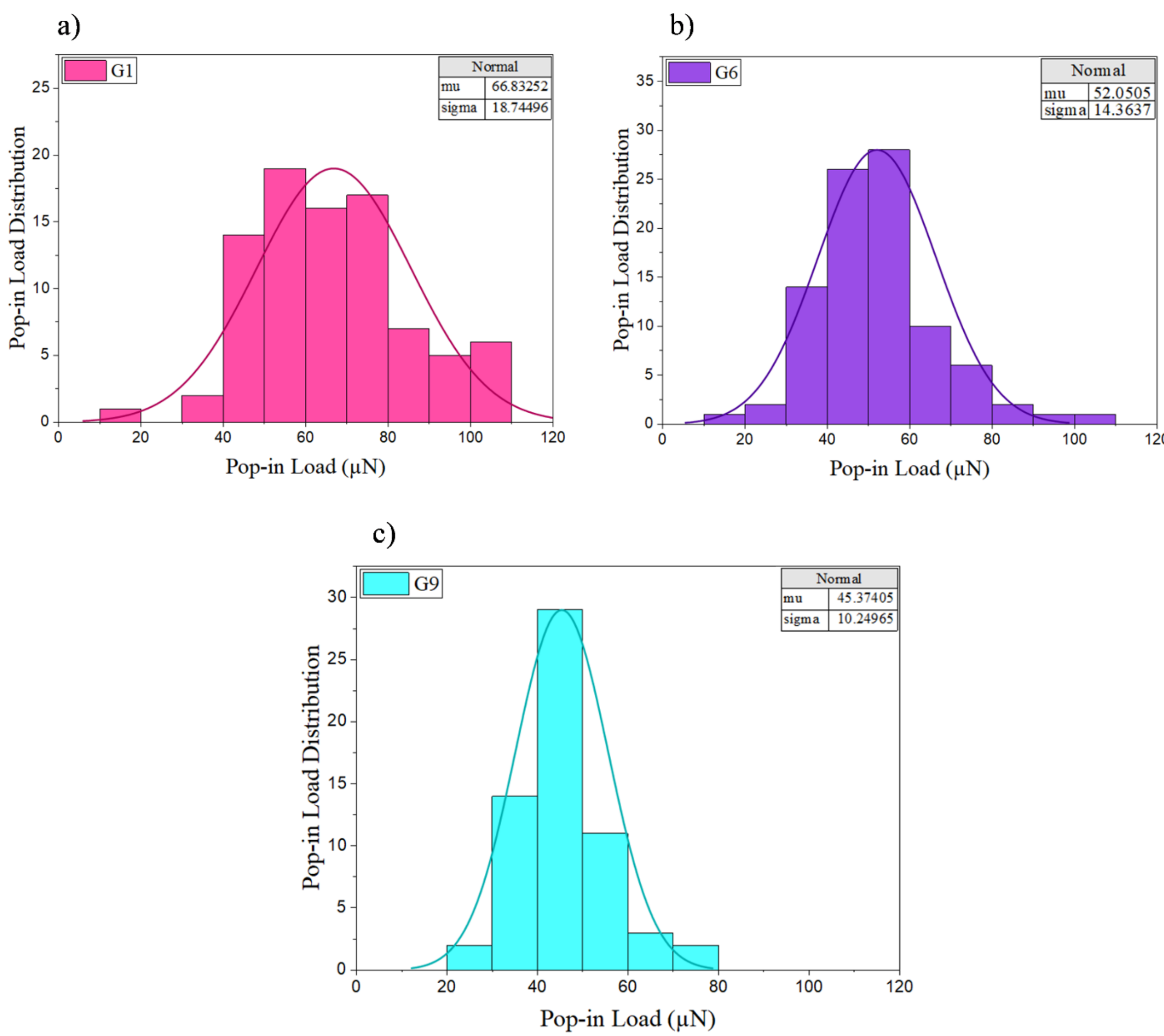

22Figure 4.4. Pop-in load distributions for selected grains (G1, G9, and G9)

Based on the pop-in modes and pop-in loads statistical evaluation all tested grain orientations have been classified into three distinct groups including: (i). Group I – basal orientations, consisting of G1 and G2, where the load direction is close to the c-axis; (ii). Group II – prismatic orientations, including G3 to G7, where the load direction is approximately normal to prismatic planes; and (iii). Group III – pyramidal orientations, encompassing G8 to G13, where the load direction is approximately normal to pyramidal planes.

The observed variations in dominant pop-in types and corresponding pop-in loads indicate the presence of distinct mechanisms governing incipient plasticity, which are further analysed in the discussion section.

4.3 Maximum shear stress at first pop-in

To quantitatively evaluate the incipient plasticity across different grain orientations, the maximum shear stress (τ_{max}) corresponding to the first pop-in event is estimated. According to the Hertzian elastic contact mechanics, the maximum contact pressure (P_0) is defined as [24]:

$$P_0 = \left(\frac{6PE_r^2}{\pi^3 R^2}\right)^{1/3} \qquad \text{Eq. 4.1}$$

Where P represents the applied load, R denotes the indenter radius, and E_r is the reduced indentation modulus calculated using Equation 2.

$$E_r = \left[\frac{1}{E_{eff}} + \frac{1-\upsilon_i^2}{E_i}\right]^{-1} \qquad \text{Eq. 4.2}$$

E_i and ν_i denote Young's modulus and Poisson's ratio of the diamond indenter, respectively, with values of 1141 GPa and 0.07. To account for elastic anisotropy, indentation elastic moduli are adopted from Catoor et al [11], which applies the method described in Gao and Pharr [115] with elastic constants provided by Slutsky and Garland [116].

In addition, the indentation Schmid factor (ISF), characterizing the crystallography of different slip systems, is defined as the ratio of resolved shear stress applied on a given slip system (α) to the maximum contact pressure [11, 98].

$$\tau_{RSS}^{(\alpha)} = ISF^{(\alpha)} \cdot P_0 \qquad \text{Eq. 4.3}$$

For simplification, we adopt the explicit solutions for the stress field, σ_{ij}, underneath a spherical indenter to estimate the resolved shear stress, $\tau_{RSS}^{(\alpha)}$, derived by Hamilton [25].

$$\tau_{RSS}^{(\alpha)} = s_i^{\alpha} \cdot m_j^{\alpha} \cdot \sigma_{ij} \qquad \text{Eq. 4.4}$$

Where s_i^{α} and m_j^{α} represent the slip direction and slip plane normal of the slip system (α), respectively. Although Hamilton's solutions assume an isotropic solid, the calculated max ISFs of ⟨a⟩- or ⟨c+a⟩- dislocations differ by <5% from the values for reported (0001), $(10\bar{1}2)$, and $(10\bar{1}0)$ orientations in [11, 98], which employ computationally intensive numerical solutions of the local stress field in an anisotropic solid like Mg. Since steep gradients in the local stress field are expected under the indenter, the mesh, used to discretize the stressed volume, must be fine enough to improve the precision of the local stress field and, consequently, the estimation of the indentation factor (ISF). The use of Hamilton's explicit solutions enables the current estimation of the ISF with the nanometer precision under the current pop-in loads.

In Table 4.2, E_{eff} for different grain orientations and *ISF* values for different slip systems including basal ⟨a⟩, prismatic ⟨a⟩, pyramidal-I ⟨c+a⟩ , and pyramidal-II ⟨c+a⟩ are listed. Accordingly, Group I (G1 and G2) exhibit the highest ISF values corresponding to the pyramidal ⟨c+a⟩ slip, followed by basal ⟨a⟩-slip. Group II (G3-G7) has the very close values for prismatic ⟨a⟩ and pyramidal ⟨c+a⟩-slip, much higher compared to basal ⟨a⟩-slip. Group III (G8-G13) have comparable *ISF* values for all slips, most having slightly higher values for basal ⟨a⟩-slip and pyramidal ⟨c+a⟩-slip.

Table 4.2: Listing the E_{eff}, ISF, and activation volume values for different dislocation modes.

Grain	**E_{eff} (GPa)**	**ISF - Basal ⟨a⟩**	**ISF – Prismatic ⟨a⟩**	**ISF - Pyramidal I ⟨c+a⟩**	**ISF - Pyramidal II ⟨c+a⟩**
G1	49.8	0.271	0.127	0.309	0.309
G2	50.25	0.220	0.133	0.290	0.302
G3	48.6	0.231	0.299	0.288	0.306
G4	48.5	0.230	0.308	0.303	0.298
G5	48.6	0.198	0.306	0.280	0.295
G6	48.5	0.243	0.286	0.306	0.271
G7	48.5	0.241	0.300	0.296	0.307
G8	48.7	0.288	0.203	0.270	0.254
G9	48.4	0.264	0.293	0.308	0.300

G10	48.4	0.274	0.275	0.305	0.283
G11	48.4	0.294	0.261	0.295	0.291
G12	48.5	0.293	0.236	0.283	0.261
G13	48.4	0.282	0.278	0.303	0.296

Figure 4.5 presents the cumulative probability of the first pop-in load and the estimated maximum resolved shear stress under different assumptions. As shown in Figure 4.5 (a), the median first pop-in load for G1 and G2 is higher than that of other grains. Figure 4.5 (b) represents τ_{max} under the anisotropic elastic modulus (E_{eff}), and the maximum possible *ISF* (0.31). Figure 4.5 (c) illustrates τ_{max}, considering the elastic anisotropy (E_{eff}) with considering the *ISF* for basal ⟨a⟩-slip. Figures 4.5 (d–f) present τ_{max}, accounting for elastic anisotropy by incorporating the indentation modulus E_{eff} and the highest *ISF* for ⟨a⟩-slip (d), *ISF* for pyramidal-II ⟨c+a⟩-slips (e), and *ISF* for all slip systems (f), respectively.

While the highest *ISF* and E_{eff} are applied for all orientations, Group I (G1 and G2), exhibit the highest resolved shear stresses over other orientations (Figure 6(e)). In contrast, when the basal ⟨a⟩ *ISF* is incorporated into the calculation (Figure 4.5(c)), a significant disparity appears in the cumulative probability curves, suggesting that basal ⟨a⟩-slip is not the dominant mechanism across all orientation ranges. However, using the maximum *ISF* for ⟨a⟩-slips, as shown in Figure 4.5(d), results in a more convergent stress distribution across all grain orientations, although basal orientations display slightly lower stress values.

Figure 4.5 (f) demonstrates that Group I (G1 and G2) have a median shear stress of around 1.3 GPa while Group II & III orientations have comparatively lower stress, with median values of approximately 1 GPa, despite only minor differences for different orientations. While considering only ⟨a⟩-slips, the G2 exhibits slightly lower shear stress levels than other grains. The variation in the maximum shear stress required for basal orientations compared to others can be attributed to the differences in dominating dislocation nucleation mechanisms.

Irrespective of the adopted *ISF* for τ_{max} calculations, that τ_{max} at the first pop-in is found to be 0.6-1.3 GPa, well falling within the range between approximately G/14 to G/30 (where G is the shear modulus). This observed stress range aligns closely with theoretical predictions for the critical shear stress necessary for dislocation nucleation in crystalline materials [43, 47, 98, 117].

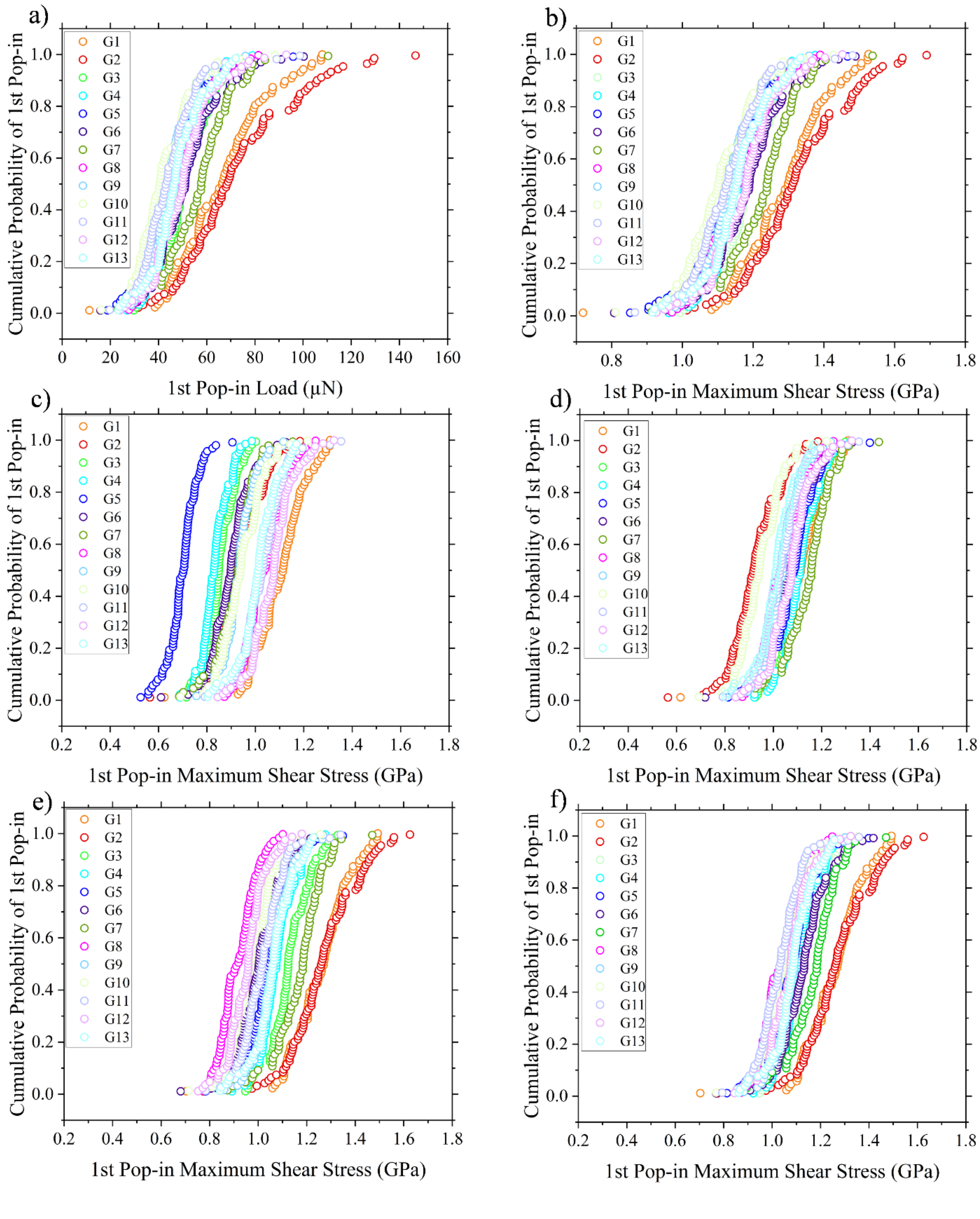

Figure 4.5. Cumulative possibility of the maximum shear stress of first pop-ins, (a) cumulative probabilities of first pop-in load, (b) Anisotropic elastic modulus (E_{eff}), ISF = 0.31, c) Anisotropic elastic modulus (E_{eff}), ISF for basal ⟨a⟩ dislocation, d) Anisotropic elastic modulus (E_{eff}), ISF for all ⟨a⟩-type dislocation, e) Anisotropic elastic modulus (E_{eff}), ISF for pyramidal-II ⟨c+a⟩ dislocation, and f) Anisotropic elastic modulus (E_{eff}), highest ISF for all types of dislocations.

4.4 Activation volume at the first pop-in

As mentioned earlier, the first pop-in is recognized as an indicator of dislocation nucleation. The statistical nature of this event can be directly correlated to the activation volume associated with the first pop-in. By analyzing the probabilistic distribution of pop-in stress, the activation volume can be obtained from the equation [47-49]:

$$V = \frac{\pi}{1.5 \times ISF} \left(\frac{3R}{4E_r}\right)^{2/3} kT\alpha \qquad \text{Eq. 4.5}$$

Where, α is a parameter obtained from the linear fit of the slope of the *ln[−ln(1−F)]* versus *P1/3* plot, as illustrated in Figure 4.6. *F* represents the cumulative probability of given stresses for the target grain.

As shown in Figure 4.6, a bimodal distribution is pronounced in basal orientations G1 and G2. This bimodal behavior likely reflects the involvement of different mechanisms of incipient plasticity at varying stress ranges [48]. However, for simplicity, we apply a linear fit for the entire distribution.

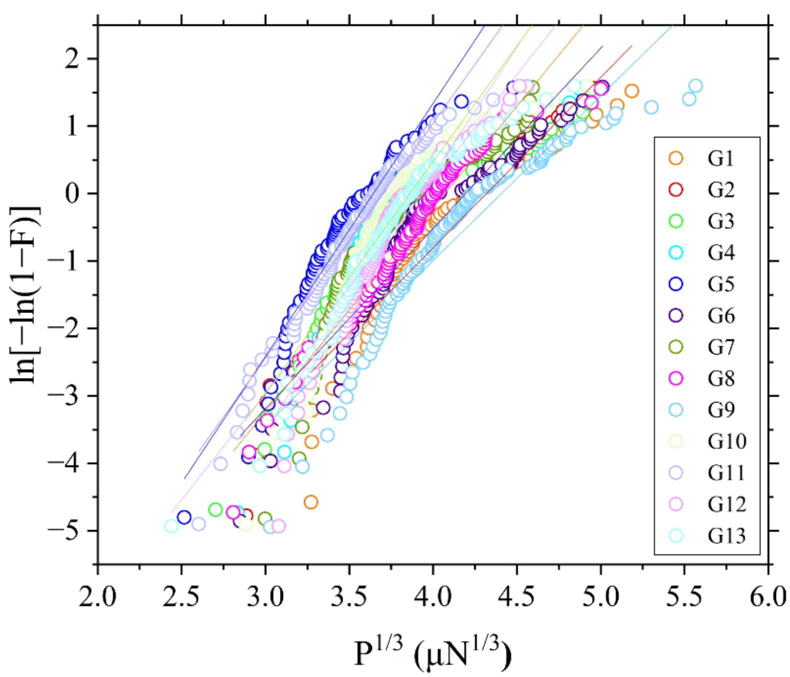

23Figure 4.6. ln[−ln(1−F)] versus P1/3 for each grain orientation including the α values.

The activation volumes corresponding to various grain orientations are presented in Table 4.3. All grains exhibit activation volumes within the range of approximately 27-40 Å^3, corresponding to 1-2 atomic volumes in Mg. The observed small activation volume, involving only 1–2 atom volume, cannot be attributed to twin nucleation, which requires a much larger activation volume, i.e., at least six atomic layers [10]. This aligns with reported literature, which indicates that a large stressed volume—arising from either a large indenter or high loads—is necessary to trigger twinning events. Consequently, we exclude twin nucleation from our analysis and attribute the first pop-in event to dislocation events.

Table 4.3..Activation volumes measured for various grain orientations, including the α value.

Grain	α	Volume (°A^3)	V/Atomic Volume
G1	2.01	27.44	1.08
G2	2.58	34.2	1.35
G3	2.46	35.26	1.39
G4	2.69	37.47	1.48
G5	2.16	30.20	1.19
G6	2.43	35.75	1.41
G7	2.18	31.02	1.22
G8	2.42	34.83	1.41
G9	2.36	34.43	1.36
G10	2.51	35.02	1.38
G11	2.45	35.28	1.4
G12	2.77	40.44	1.6
G13	2.71	29.58	1.17

4.5. Possible dislocation nucleation mechanism

The estimated activation volume, across all grain orientations, is approximately 27-40 Å^3 (0.8-1.2 b^3), which is slightly higher than the reported values for indentation on the (0001) and $(10\bar{1}0)$ Mg [15] and falls within the range for other metals [50]. The indentation behaviours of the current alloy are expected to resemble that of single-crystal Mg [11, 15], as the current alloy is annealed at 500°C for 8 hours, and the stressed volume under each indentation is much smaller than the grain size. As a result, the influence of grain boundaries, twin boundaries, or pre-existing dislocations, can be considered negligible. Atomistic simulations on FCC metals, such as Au and Ni_3Al stressed within small volumes, suggest that a single atom can achieve a critical displacement, under large applied strains, serving as the initialization site for dislocation [48, 75]. This process, which can be promoted at the surface, falls within the activation volume range of 1-10 b^3 [54]. While dislocation nucleation can also be facilitated by point defects, such as vacancies or solutes, the changes in the activation volumes is minimal, as reported in doped high-entropy alloys [41] and Mg alloyed with Li, Al, Zn, and Y [20]. Moreover, it is observed that the Gd solute in such heat treatment can segregate more in grain boundaries [118]. This indicates that the Gd likely has a negligible influence on the activation volumes for dislocation nucleation in the current alloy. In short, the surface dislocation nucleation is likely to be the predominant mechanism.

4.6. Early stage of incipient plasticity

As presented in Table 4.1, most p-h curves exhibit either excursions or deviations before the first pop-ins for all grains. Atomistic simulations of multiple materials suggest that the initial dislocation structure underneath the indenter usually consists of dislocation semi-loops emerging at the surface [68], where local shear stresses approach the material's theoretical strength [50]. The formation of a semi-loop can produce small displacements, which, in addition to appearing as excursions, can also lead to slight deviations from the Hertzian fit [15]. Atomistic simulations of indentation on the (0001) and $(10\bar{1}0)$ Mg confirm that the semi-loops are basal ⟨a⟩-dislocations, the easiest slip system [15, 105]. We speculate that such semi-loops are basal ⟨a⟩- dislocations for all grains. Theoretically, the shear stress associated with excursions and deviations should be identical across all grains. However, the experimental measurement can be largely scattered since the formation of semi-loops largely depended on the surface conditions, in addition to the local stress fields. In addition, deviations are likely ill-defined in recorded p-h curves, leading to scattered comparisons in the measured shear stress for excursions and deviations.

The first pop-ins, characterized by significant displacement bursts, are attributed to dislocation nucleation producing full loops, slipping into the bulk lattice [15, 32]. The above semi-loops can act as precursors for the formation of full loops via either the transition of basal to pyramidal ⟨c+a⟩ slip, and/or basal to prismatic ⟨a⟩ cross-slip mechanisms [15]. The occurrence of basal-to-prismatic cross-slip has been reported in other modelling studies [119, 120]. As indicated by Figure 4.5(f), the cumulative probability curves for the first pop-in converge when the load is normalized to the maximum *ISF* of all slip systems. The scatter in these curves is likely due to the varying possibility of multiple cross-slip modes existing in individual grains. Group I (G1 and G2) exhibit slightly higher stresses, as a significant fraction of pyramidal ⟨c+a⟩-slip, which requires higher stress due to the larger Burgers vector, is expected to compensate for the c-axis deformation.

4.7. Possible mechanism for successive pop-in mechanism in C-axis orientations

In addition, almost every p-h curve for Group I (G1 and G2) exhibits successive pop-ins (Figure 4.1). Similar successive pop-ins have been typically reported in both experimental and simulation studies of indentation normal to the {111} plane of FCC metals like aluminium (Al) [32] and gold (Au) [68], and the basal plane of Mg [15]. The surface dislocation semi-loops, that correspond to the excursions, can evolve into immobile Lomer-Cottrell locks via dislocation cross-slip in FCC metals, re-enabling elastic deformation between successive pop-ins [86]. Like the Lomer-Cottrell lock, the basal-pyramidal dislocation lock has been reported in Mg while ⟨a⟩ and ⟨c+a⟩ dislocations interact [68, 121, 122]. This interaction and resulting successive pop-ins, is expected to predominate in Group I (G1 and G2) grains compared to the others, as suggested by the proposed dislocation nucleation mechanisms.

4.8. Conclusion

In summary, nanoindentation experiments were conducted on 13 grains of a coarse-grained Mg-2 wt.% Gd alloy, encompassing basal, prismatic, and pyramidal orientations. The findings provide significant insights into the orientation-dependent incipient plasticity of this alloy:

1. During incipient plasticity, three first pop-in modes were identified: (i) ideal pop-in, (ii) pop-in with deviation, and (iii) pop-in with excursion. Statistical analysis reveals a strong orientation dependence. Grains G1 and G2, whose loading directions are nearly perpendicular to the basal plane, displayed excursions (mode iii) in about half of their load-displacement curves. In contrast, grains G3–G13 predominantly showed deviations (mode ii), except for G5, which exhibited an ideal pop-in (mode i) in 68% of cases.

2. Basal orientations exhibit a higher median shear stress (~1.3 GPa) compared to prismatic and pyramidal orientations (~1 GPa). The measured shear stress aligns well with theoretical values for dislocation nucleation (G/14 to G/30). The difference is attributed to the involvement of pyramidal ⟨c+a⟩ dislocations for basal orientations, which accommodate plastic deformation along the c-axis.

3. Load-displacement curves preceding the first pop-in reveal minor excursions and slight deviations from Hertz fitting. These behaviors are consistent with the nucleation of semi-loop basal ⟨a⟩ dislocations at the surface, representing the early stages of incipient plasticity and serving as precursors for developing full loops, corroborating atomistic simulations in the literature. The first pop-ins are attributed to the transition of surface semi-loops into either ⟨a⟩-slip or pyramidal ⟨c+a⟩-slip via cross-slip.

4. The activation volume associated with the first pop-in event across different grain orientations falls within the range of 27 to 40 $Å^3$, roughly equivalent to the volume of about two atoms. This is consistent with values reported in simulations, reinforcing the likelihood of a surface dislocation nucleation mechanism. Additionally, the small size of this activation volume is insufficient to support twinning, which, based on atomistic models, generally involves the collective movement of six or more atomic layers.

5. The exclusive appearance of successive pop-ins in basal orientations highlights orientation-dependent incipient plasticity in HCP metals, reported here for the first time. This behavior likely stems from a basal–pyramidal dislocation lock involving ⟨a⟩ and ⟨c+a⟩ dislocations, similar to the Lomer–Cottrell lock in FCC metals. It also supports the nucleation of pyramidal ⟨c+a⟩ dislocations along the c-axis in magnesium, aligning with atomistic simulation findings in the literature.

Chapter 5 – Conclusion and future work

5.1. Summary of Conclusion

In summary, nanoindentation experiments were conducted on 13 grains of a coarse-grained Mg-2 wt.% Gd alloy, encompassing basal, prismatic, and pyramidal orientations. The findings provide significant insights into the orientation-dependent incipient plasticity of this alloy:

1- A stress-free surface of Mg-Gd alloys was successfully prepared using only mechanical polishing with a 0.05 μm polycrystalline diamond glycol-based suspension. This approach eliminates the need for chemical etching, which is commonly utilized in the literature. Our findings demonstrate that an etch-free procedure yields a stress-free surface with a high confidence index for EBSD analyses, as well as a smooth, mirror-like finish suitable for the nanoindentation measurements.

2- The nanoindentation experiment was successfully designed to investigate dislocation-based incipient plasticity by minimizing the indented volume. Applying a 1000 μN load resulted in distinct pop-in events occurring at low loads (<100 μN) and shallow displacements (approximately 10–20 nm). This significantly reduced the indented volume and, consequently, minimized the likelihood of twinning nucleation. Surface probe microscopy (SPM) and high-resolution scanning electron microscopy (HRSEM) analyses on five different grain orientations revealed no evidence of twinning traces, showing only a few scratches likely formed during sample preparation. . .

3- By employing a precise grain identification approach called "grain signing-finding approach", nanoindentation experiments were successfully conducted on 13 different grain orientations, with more than 100 indents per orientation. This approach can be applied to other alloy systems to investigate a wide range of grain orientations and their mechanical responses via nanoindentation.

4- During the early stages of incipient plasticity, three distinct modes of the first pop-in were identified: (i) an ideal first pop-in, (ii) a first pop-in with deviation, and (iii) a first pop-in with excursion. Statistical analysis indicates that these modes depend strongly on grain orientation. Specifically, grains G1 and G2, with loading directions nearly perpendicular to the basal plane, exhibited excursions (mode iii) in approximately 50% of their load-displacement (p-h) curves prior to the first pop-in. By contrast, grains G3–G13 primarily displayed deviations before the first pop-in (mode ii) in more than half of their p-h curves, with the exception of grain G5, which showed an ideal pop-in (mode i) in 68% of the cases.

5- Basal orientations exhibit a higher median shear stress (~1.3 GPa) compared to prismatic and pyramidal orientations (~1 GPa). The measured shear stress aligns well with theoretical values for dislocation nucleation (G/14 to G/30). The difference is attributed to the involvement of pyramidal ⟨c+a⟩ dislocations for basal orientations, which is needed to accommodate plastic deformation along the c-axis.

6- The activation volume for the first pop-in across all grain orientations ranges from 27 to 40 Å^3, corresponding to approximately ∼2 atoms. This range aligns with simulations in the literature, supporting a surface dislocation nucleation mechanism. Furthermore, this activation volume is notably too small to support twin nucleation, which typically requires the coordinated motion of at least six atomic layers according to atomistic models.

7- Load-displacement curves preceding the first pop-in reveal minor excursions and slight deviations from Hertz fitting. These behaviors are consistent with the nucleation of semi-loop basal ⟨a⟩ dislocations at the surface, representing the early stages of incipient plasticity and serving as precursors for developing full loops, corroborating atomistic simulations in the literature.

8- The exclusive observation of successive pop-ins in basal orientations provides new evidence of the orientation dependence of incipient plasticity, reported here for the first time in HCP metals. This behavior, inspired by atomistic simulations of magnesium under deformation, may result from a basal–pyramidal dislocation lock, which occurs when ⟨a⟩ and ⟨c+a⟩ dislocations interact—an interaction previously reported in magnesium. This phenomenon is analogous to the Lomer–Cottrell lock observed in FCC crystals, which also leads to successive pop-ins during incipient plasticity. Furthermore, this behavior supports the involvement of a the nucleation of pyramidal ⟨c+a⟩ dislocations along the c-axis in magnesium.

5.2. Suggestions for future work

Building on the orientation-dependent incipient plasticity observed in Mg-Gd alloys, future research should clarify the early stages of plastic deformation to elucidate the underlying dislocation mechanisms across various orientations.

1- Cross-Sectional TEM Analysis Post-Indentation:

Conducting cross-sectional transmission electron microscopy (TEM) immediately after the first pop-in event without extra plastic deformation would enable direct observation of dislocation structures and potential cross-slip mechanisms. This real-time structural information can validate atomistic models and enhance our understanding of the fundamental processes triggering incipient plasticity.

2- Atomistic Simulations for Different Orientations:

Although this study highlights orientation-dependent incipient plasticity in Mg-Gd alloys, comprehensive atomistic simulations are needed to elucidate the detailed mechanisms underlying dislocation nucleation in various orientations. In particular, focusing on early stage of basal orientations—which exhibited successive pop-ins—could provide a deeper understanding of the atomistic processes governing incipient plasticity under different loading directions.

3- Role of Grain Boundaries in Nano-Grained Alloys:

Investigating the same Mg-Gd alloy at the nano-grain scale could clarify the influence of grain boundaries on incipient plasticity. By systematically varying grain size, researchers can determine how boundary characteristics (e.g., misorientation, boundary type) interact with dislocation nucleation, pop-in events, and overall plastic deformation.

References

[1] M.O. Pekguleryuz, K. Kainer, A.A. Kaya, Fundamentals of magnesium alloy metallurgy, Elsevier2013.
[2] S.E. Prameela, P. Yi, Y. Hollenweger, B. Liu, J. Chen, L. Kecskes, D.M. Kochmann, M.L. Falk, T.P. Weihs, Strengthening magnesium by design: Integrating alloying and dynamic processing, Mechanics of Materials 167 (2022) 104203.
[3] J. Tan, S. Ramakrishna, Applications of magnesium and its alloys: A review, Applied Sciences 11(15) (2021) 6861.
[4] Y. Yang, X. Xiong, J. Chen, X. Peng, D. Chen, F. Pan, Research advances of magnesium and magnesium alloys worldwide in 2022, Journal of Magnesium and Alloys (2023).
[5] Y. Liu, D. Yu, Y. Zhang, J. Zhou, D. Sun, H. Li, Research advances on weldability of Mg alloy and other metals worldwide in recent 20 years, Journal of Materials Research and Technology 25 (2023) 3458-3481.
[6] A.A. Luo, Magnesium casting technology for structural applications, journal of Magnesium and Alloys 1(1) (2013) 2-22.
[7] S.P. Kanti, R. Kumar, S. Panigrahi, B. Sahoo, Effect of rolling reduction on microstructure and tension-compression yield asymmetry of rolled AZ31 magnesium sheet, Materials Science and Engineering: A 903 (2024) 146683.
[8] J. Li, Q. Huo, C. Wang, Y. Zhang, Z. Zhang, G. Feng, X. Yang, Tension-compression asymmetry in hot-rolled Mg-3wt% Gd alloy under creep loading, Materials Science and Engineering: A 831 (2022) 142124.
[9] X. Lin, Z. Chen, J. Shao, J. Xiong, Z. Hu, C. Liu, Deformation mechanism, orientation evolution and mechanical properties of annealed cross-rolled Mg-Zn-Zr-Y-Gd sheet during tension, Journal of Magnesium and Alloys 11(7) (2023) 2340-2350.
[10] X. Li, Q. Zeng, J. Wang, Twinning dynamics in nanoscale body-centered cubic tungsten, Scripta Materialia 220 (2022) 114930.
[11] D. Catoor, Y. Gao, J. Geng, M. Prasad, E. Herbert, K. Kumar, G.M. Pharr, E.P. George, Incipient plasticity and deformation mechanisms in single-crystal Mg during spherical nanoindentation, Acta materialia 61(8) (2013) 2953-2965.
[12] J. Cheng, Twinning during nanoindentation of magnesium single crystals, Deakin University, 2019.
[13] J. Cheng, T. Guo, M.R. Barnett, Influence of temperature on twinning dominated pop-ins during nanoindentation of a magnesium single crystal, Journal of Magnesium and Alloys 10(1) (2022) 169-179.
[14] H. Somekawa, C.A. Schuh, Effect of crystal orientation on nanoindentation behavior in magnesium, Metallurgical and Materials Transactions A 47 (2016) 3227-3234.
[15] H. Somekawa, T. Tsuru, A. Singh, S. Miura, C.A. Schuh, Effect of crystal orientation on incipient plasticity during nanoindentation of magnesium, Acta Materialia 139 (2017) 21-29.
[16] C. Anthony, Fischer-Cripps, Nanoindentation, Springer New York, 2011.
[17] J. Nemecek, Nanoindentation in Materials Science, BoD–Books on Demand2012.
[18] I. Sen, S.S. Kumar, Characterizing stress-strain behavior of materials through nanoindentation, Elasticity of materials, IntechOpen2021.
[19] T. Tsui, M. Pharr, Advanced Nanoindentation in Materials, MDPI2018.
[20] K. Gan, D. Yan, S. Zhu, Z. Li, Interstitial effects on the incipient plasticity and dislocation behavior of a metastable high-entropy alloy: nanoindentation experiments and statistical modeling, Acta Materialia 206 (2021) 116633.
[21] B. Shi, C. Yang, Y. Peng, F. Zhang, F. Pan, Anisotropy of wrought magnesium alloys: A focused overview, Journal of Magnesium and Alloys 10(6) (2022) 1476-1510.
[22] A.C. Fischer-Cripps, Nanoindentation [electronic resource], (2011).
[23] H. Hertz, The contact of elastic solids, J Reine Angew, Math 92 (1881) 156-171.
[24] K.L. Johnson, Contact mechanics, Cambridge university press1987.
[25] A.C. Fischer-Cripps, Introduction to contact mechanics, Springer2007.
[26] R. Han, J. Chen, A modified Sneddon model for the contact between conical indenters and spherical samples, Journal of Materials Research 36(8) (2021) 1762-1771.

[27] W.C. Oliver, G.M. Pharr, An improved technique for determining hardness and elastic modulus using load and displacement sensing indentation experiments, Journal of materials research 7(6) (1992) 1564-1583.
[28] B. Poon, D. Rittel, G. Ravichandran, An analysis of nanoindentation in linearly elastic solids, International Journal of Solids and Structures 45(24) (2008) 6018-6033.
[29] G. Wang, X. Niu, Nanoindentation of soft solids by a flat punch, Acta Mechanica Sinica 31 (2015) 531-535.
[30] A. Gouldstone, N. Chollacoop, M. Dao, J. Li, A.M. Minor, Y.-L. Shen, Indentation across size scales and disciplines: Recent developments in experimentation and modeling, Acta Materialia 55(12) (2007) 4015-4039.
[31] C. Schuh, T. Nieh, A survey of instrumented indentation studies on metallic glasses, Journal of Materials Research 19 (2004) 46-57.
[32] J. Li, K.J. Van Vliet, T. Zhu, S. Yip, S. Suresh, Atomistic mechanisms governing elastic limit and incipient plasticity in crystals, Nature 418(6895) (2002) 307-310.
[33] K.J. Van Vliet, J. Li, T. Zhu, S. Yip, S. Suresh, Quantifying the early stages of plasticity through nanoscale experiments and simulations, Physical Review B 67(10) (2003) 104105.
[34] Y. Rahmani, R. Koopman, D. Denisov, P. Schall, Probing incipient plasticity by indenting colloidal glasses, Scientific Reports 3(1) (2013) 1064.
[35] E. Tadmor, R. Miller, R. Phillips, M. Ortiz, Nanoindentation and incipient plasticity, Journal of Materials Research 14(6) (1999) 2233-2250.
[36] J.-Q. Hu, Z.-L. Liu, Y.-N. Cui, F.-X. Liu, Z. Zhuang, A New View of Incipient Plastic Instability during Nanoindentation, Chinese Physics Letters 34(4) (2017) 046101.
[37] J. Pethica, W. Oliver, Mechanical properties of nanometre volumes of material: use of the elastic response of small area indentations, MRS Online Proceedings Library (OPL) 130 (1988) 13.
[38] A. Cottrell, Dislocations and Plastic Flow in Crystals Oxford Univ, Press, ld&3 (1953).
[39] L. Ma, D.J. Morris, S.L. Jennerjohn, D.F. Bahr, L.E. Levine, The role of probe shape on the initiation of metal plasticity in nanoindentation, Acta materialia 60(12) (2012) 4729-4739.
[40] S. Ogata, J. Li, N. Hirosaki, Y. Shibutani, S. Yip, Ideal shear strain of metals and ceramics, Physical Review B—Condensed Matter and Materials Physics 70(10) (2004) 104104.
[41] H. Somekawa, C.A. Schuh, Effect of solid solution elements on nanoindentation hardness, rate dependence, and incipient plasticity in fine grained magnesium alloys, Acta materialia 59(20) (2011) 7554-7563.
[42] S. Suresh, T.-G. Nieh, B. Choi, Nano-indentation of copper thin films on silicon substrates, Scripta Materialia 41(9) (1999) 951-957.
[43] C. Zhu, Z. Lu, T. Nieh, Incipient plasticity and dislocation nucleation of FeCoCrNiMn high-entropy alloy, Acta Materialia 61(8) (2013) 2993-3001.
[44] D.F. Bahr, D. Kramer, W. Gerberich, Non-linear deformation mechanisms during nanoindentation, Acta materialia 46(10) (1998) 3605-3617.
[45] S. Syed Asif, J. Pethica, Nanoindentation creep of single-crystal tungsten and gallium arsenide, Philosophical Magazine A 76(6) (1997) 1105-1118.
[46] T. Li, Y. Gao, H. Bei, E.P. George, Indentation Schmid factor and orientation dependence of nanoindentation pop-in behavior of NiAl single crystals, Journal of the Mechanics and Physics of Solids 59(6) (2011) 1147-1162.
[47] C.A. Schuh, A.C. Lund, Application of nucleation theory to the rate dependence of incipient plasticity during nanoindentation, Journal of Materials research 19(7) (2004) 2152-2158.
[48] Y. Gao, H. Bei, Strength statistics of single crystals and metallic glasses under small stressed volumes, Progress in Materials Science 82 (2016) 118-150.
[49] S.-P. Wang, J. Xu, Incipient plasticity and activation volume of dislocation nucleation for TiZrNbTaMo high-entropy alloys characterized by nanoindentation, Journal of Materials Science & Technology 35(5) (2019) 812-816.

[50] J. Mason, A. Lund, C. Schuh, Determining the activation energy and volume for the onset of plasticity during nanoindentation, Physical Review B—Condensed Matter and Materials Physics 73(5) (2006) 054102.
[51] W.-W. Pang, P. Zhang, G.-C. Zhang, A.-G. Xu, X.-G. Zhao, Dislocation creation and void nucleation in FCC ductile metals under tensile loading: A general microscopic picture, Scientific reports 4(1) (2014) 6981.
[52] Y. Ye, Z. Lu, T. Nieh, Dislocation nucleation during nanoindentation in a body-centered cubic TiZrHfNb high-entropy alloy, Scripta Materialia 130 (2017) 64-68.
[53] A.T. Jennings, J.R. Greer, Heterogeneous dislocation nucleation from surfaces and interfaces as governing plasticity mechanism in nanoscale metals, Journal of Materials Research 26(22) (2011) 2803-2814.
[54] T. Zhu, J. Li, A. Samanta, A. Leach, K. Gall, Temperature and strain-rate dependence of surface dislocation nucleation, Physical Review Letters 100(2) (2008) 025502.
[55] F. Dominguez-Gutierrez, P. Grigorev, A. Naghdi, Q. Xu, J. Byggmastar, G. Wei, T. Swinburne, S. Papanikolaou, M. Alava, Atomistic simulations of nanoindentation in single crystalline tungsten: The role of interatomic potentials, arXiv preprint arXiv:2205.09165 (2022).
[56] E. Lilleodden, J. Zimmerman, S. Foiles, W. Nix, Atomistic simulations of elastic deformation and dislocation nucleation during nanoindentation, Journal of the Mechanics and Physics of Solids 51(5) (2003) 901-920.
[57] I. Stachiv, J. Zapomel, Y.-L. Chen, Simultaneous determination of the elastic modulus and density/thickness of ultrathin films utilizing micro-/nanoresonators under applied axial force, Journal of Applied Physics 115(12) (2014).
[58] C.A. Volkert, E.T. Lilleodden, Size effects in the deformation of sub-micron Au columns, Philosophical Magazine 86(33-35) (2006) 5567-5579.
[59] A. Gouldstone, K.J. Van Vliet, S. Suresh, Simulation of defect nucleation in a crystal, Nature 411(6838) (2001) 656-656.
[60] K. Jin, Y. Xia, M. Crespillo, H. Xue, Y. Zhang, Y. Gao, H. Bei, Quantifying early stage irradiation damage from nanoindentation pop-in tests, Scripta Materialia 157 (2018) 49-53.
[61] J.R. Morris, H. Bei, G.M. Pharr, E.P. George, Size effects and stochastic behavior of nanoindentation pop in, Physical review letters 106(16) (2011) 165502.
[62] T. Ohmura, M. Wakeda, Pop-in phenomenon as a fundamental plasticity probed by nanoindentation technique, Materials 14(8) (2021) 1879.
[63] F. Pöhl, Pop-in behavior and elastic-to-plastic transition of polycrystalline pure iron during sharp nanoindentation, Scientific reports 9(1) (2019) 15350.
[64] Y. Sato, S. Shinzato, T. Ohmura, T. Hatano, S. Ogata, Unique universal scaling in nanoindentation pop-ins, Nature Communications 11(1) (2020) 4177.
[65] Y. Zhao, J.-M. Park, J.-i. Jang, U. Ramamurty, Bimodality of incipient plastic strength in face-centered cubic high-entropy alloys, Acta Materialia 202 (2021) 124-134.
[66] D. Bahr, D. Wilson, D. Crowson, Energy considerations regarding yield points during indentation, Journal of Materials Research 14(6) (1999) 2269-2275.
[67] Y.-J. Chiu, Y.-H. Yao, D. Dimitrov, J.-Y. Juang, S.-R. Jian, Unveiling the Deformation Behaviors of Luvo4 Single Crystal by Using Nanoindentation and Finite Element Analysis, Available at SSRN 5056462.
[68] C.L. Kelchner, S. Plimpton, J. Hamilton, Dislocation nucleation and defect structure during surface indentation, Physical review B 58(17) (1998) 11085.
[69] J. Kiely, J. Houston, Nanomechanical properties of Au (111),(001), and (110) surfaces, Physical Review B 57(19) (1998) 12588.
[70] J. Knap, M. Ortiz, Effect of indenter-radius size on Au (001) nanoindentation, Physical Review Letters 90(22) (2003) 226102.
[71] D. Lorenz, A. Zeckzer, U. Hilpert, P. Grau, H. Johansen, H. Leipner, Pop-in effect as homogeneous nucleation of dislocations during nanoindentation, Physical review B 67(17) (2003) 172101.

[72] R.E. Miller, L. Shilkrot, W.A. Curtin, A coupled atomistics and discrete dislocation plasticity simulation of nanoindentation into single crystal thin films, Acta Materialia 52(2) (2004) 271-284.
[73] N. Tymiak, A. Daugela, T. Wyrobek, O. Warren, Acoustic emission monitoring of the earliest stages of contact-induced plasticity in sapphire, Acta materialia 52(3) (2004) 553-563.
[74] W. Wang, C. Jiang, K. Lu, Deformation behavior of Ni3Al single crystals during nanoindentation, Acta materialia 51(20) (2003) 6169-6180.
[75] L. Zuo, A. Ngan, G. Zheng, Size dependence of incipient dislocation plasticity in Ni 3 Al, Physical review letters 94(9) (2005) 095501.
[76] S. Pathak, J.L. Riesterer, S.R. Kalidindi, J. Michler, Understanding pop-ins in spherical nanoindentation, Applied Physics Letters 105(16) (2014).
[77] G.M. Pharr, E.G. Herbert, Y. Gao, The indentation size effect: a critical examination of experimental observations and mechanistic interpretations, Annual Review of Materials Research 40(1) (2010) 271-292.
[78] S.Z. Chavoshi, S. Xu, Nanoindentation/scratching at finite temperatures: Insights from atomistic-based modeling, Progress in Materials Science 100 (2019) 1-20.
[79] Y. Lee, J.Y. Park, S.Y. Kim, S. Jun, S. Im, Atomistic simulations of incipient plasticity under Al (1 1 1) nanoindentation, Mechanics of Materials 37(10) (2005) 1035-1048.
[80] J. Zimmerman, C. Kelchner, P. Klein, J. Hamilton, S. Foiles, Surface step effects on nanoindentation, Physical Review Letters 87(16) (2001) 165507.
[81] A. Gouldstone, H.-J. Koh, K.-Y. Zeng, A. Giannakopoulos, S. Suresh, Discrete and continuous deformation during nanoindentation of thin films, Acta Materialia 48(9) (2000) 2277-2295.
[82] E. Lilleodden, W. Nix, Microstructural length-scale effects in the nanoindentation behavior of thin gold films, Acta Materialia 54(6) (2006) 1583-1593.
[83] Y. Shibutani, T. Tsuru, A. Koyama, Nanoplastic deformation of nanoindentation: Crystallographic dependence of displacement bursts, Acta materialia 55(5) (2007) 1813-1822.
[84] S. Shim, H. Bei, E.P. George, G.M. Pharr, A different type of indentation size effect, Scripta Materialia 59(10) (2008) 1095-1098.
[85] Y. Xia, Y. Gao, G.M. Pharr, H. Bei, Single versus successive pop-in modes in nanoindentation tests of single crystals, Journal of Materials Research 31(14) (2016) 2065-2075.
[86] N. Zhou, K.I. Elkhodary, X. Huang, S. Tang, Y. Li, Dislocation structure and dynamics govern pop-in modes of nanoindentation on single-crystal metals, Philosophical Magazine 100(12) (2020) 1585-1606.
[87] M.M. Biener, J. Biener, A.M. Hodge, A.V. Hamza, Dislocation nucleation in bcc Ta single crystals studied by nanoindentation, Physical Review B—Condensed Matter and Materials Physics 76(16) (2007) 165422.
[88] B. Selvarajou, J.-H. Shin, T.K. Ha, I.-s. Choi, S.P. Joshi, H.N. Han, Orientation-dependent indentation response of magnesium single crystals: modeling and experiments, Acta materialia 81 (2014) 358-376.
[89] W. Yao, P. Wang, A. Manhard, C.E. Krill III, J.-H. You, Effect of hydrogen on the slip resistance of tungsten single crystals, Materials Science and Engineering: A 559 (2013) 467-473.
[90] B.D. Beake, S. Goel, Incipient plasticity in tungsten during nanoindentation: Dependence on surface roughness, probe radius and crystal orientation, International Journal of Refractory Metals and Hard Materials 75 (2018) 63-69.
[91] F. Domínguez-Gutiérrez, S. Papanikolaou, A. Esfandiarpour, P. Sobkowicz, M. Alava, Nanoindentation of single crystalline Mo: Atomistic defect nucleation and thermomechanical stability, Materials Science and Engineering: A 826 (2021) 141912.
[92] M. Bagheripoor, Incipient deformation of small volumes of fcc metals, The University of Western Ontario (Canada), 2020.
[93] M. Bagheripoor, R. Klassen, The effect of crystal anisotropy and pre-existing defects on the incipient plasticity of FCC single crystals during nanoindentation, Mechanics of Materials 143 (2020) 103311.
[94] B. Shiari, R.E. Miller, W.A. Curtin, Coupled atomistic/discrete dislocation simulations of nanoindentation at finite temperature, (2005).
[95] K.L. Murty, Effect of c/a-ratio on crystallographic texture and mechanical anisotropy of hexagonal close packed metals, Materials Science Forum, 2003, pp. 3575-3580.

[96] J. Kwon, Characterization of deformation mechanisms in pre-strained NiAl-Mo composites and α-Ti alloy, The Ohio State University, 2012.
[97] J. Kwon, M. Brandes, P.S. Phani, A. Pilchak, Y. Gao, E.P. George, G.M. Pharr, M. Mills, Characterization of deformation anisotropies in an α-Ti alloy by nanoindentation and electron microscopy, Acta Materialia 61(13) (2013) 4743-4756.
[98] W. Zhang, Y. Gao, Y. Xia, H. Bei, Indentation Schmid factor and incipient plasticity by nanoindentation pop-in tests in hexagonal close-packed single crystals, Acta Materialia 134 (2017) 53-65.
[99] C. Barrett, M. Tschopp, H. El Kadiri, B. Li, Influence of crystallographic orientation on twin nucleation in single crystal magnesium, Magnesium Technology 2011 (2016) 295-299.
[100] P. Salunke, M. Joshi, V. Chaswal, G. Zhang, L.A. Rosenbaum, K. Dowling, P. Decker, V. Shanov, Magnesium single crystals for biomedical applications grown in vertical Bridgman apparatus, Review of Scientific Instruments 87(10) (2016).
[101] Y. Liu, N. Li, M.A. Kumar, S. Pathak, J. Wang, R.J. Mccabe, N.A. Mara, C.N. Tome, Experimentally quantifying critical stresses associated with basal slip and twinning in magnesium using micropillars, Acta Materialia 135 (2017) 411-421.
[102] T. Guo, Q. Chao, F. Siska, J. Cheng, R.R. Varma, M.R. Barnett, Analysing single twinning events in Mg-6Zn using nanoindentation, Journal of Alloys and Compounds 768 (2018) 510-516.
[103] T. Guo, F. Siska, M. Barnett, Distinguishing between slip and twinning events during nanoindentation of magnesium alloy AZ31, Scripta Materialia 110 (2016) 10-13.
[104] R. Sánchez-Martín, M. Pérez-Prado, J. Segurado, J. Molina-Aldareguia, Effect of indentation size on the nucleation and propagation of tensile twinning in pure magnesium, Acta Materialia 93 (2015) 114-128.
[105] P. Goswami, S. Pal, M. Gupta, Investigation of point defect evolution and Voronoi cluster analysis for magnesium during nanoindentation, Journal of Magnesium and Alloys 11(3) (2023) 1029-1042.
[106] G. Nayyeri, W.J. Poole, C.W. Sinclair, S. Zaefferer, P.J. Konijnenberg, C. Zambaldi, An instrumented spherical indentation study on high purity magnesium loaded nearly parallel to the c-axis, Materials Science and Engineering: A 670 (2016) 132-145.
[107] T. Guo, F. Siska, J. Cheng, M. Barnett, Initiation of basal slip and tensile twinning in magnesium alloys during nanoindentation, Journal of Alloys and Compounds 731 (2018) 620-630.
[108] Y. Liu, J. Yan, D. Xie, Y. Shen, J. Wang, G.-z. Zhu, Self-patterning screw< c> dislocations in pure Mg, Scripta Materialia 191 (2021) 86-89.
[109] Z. Wang, J. Wang, X. Lin, L. Feng, L. Ouyang, C. Dai, W. Yang, W. Huang, F. Pan, Effect of heat treatment on microstructure evolution and strengthening-toughening behavior of high-strength Mg-Gd-Y-Zn-Zr alloy fabricated by wire-arc additive manufacturing, Journal of Materials Research and Technology 31 (2024) 1896-1911.
[110] Q. Wu, Y. Wu, Q. Deng, C. Ding, Y. Zhang, N. Peng, L. Jia, Z. Chang, L. Peng, Effect of Gd content on microstructure and mechanical properties of Mg-xGd-Zr alloys via semicontinuous casting, Journal of Magnesium and Alloys (2024).
[111] A.J. Schwartz, M. Kumar, B.L. Adams, D.P. Field, Electron backscatter diffraction in materials science, Springer2009.
[112] J. Cheng, Twinning during nanoindentation of Mg single crystals, Deakin University, Deakin University, 2019.
[113] W.H. El-Garaihy, A. BaQais, A.I. Alateyah, M.F. Alsharekh, M.O. Alawad, M. Shaban, F.N. Alsunaydih, M. Kamel, The impact of ECAP parameters on the structural and mechanical behavior of pure Mg: A combination of experimental and machine learning approaches, Applied Sciences 13(10) (2023) 6279.
[114] H. Zhang, F. De Luca, H. Wang, K. Mingard, M. Gee, Deformation mechanism of WC single crystals under nanoindentation: Effects of surface defects and orientation on pop-in and hysteresis, International Journal of Refractory Metals and Hard Materials 106 (2022) 105850.
[115] Y. Gao, G.M. Pharr, Multidimensional contact moduli of elastically anisotropic solids, Scripta materialia 57(1) (2007) 13-16.

[116] L.J. Slutsky, C. Garland, Elastic constants of magnesium from 4.2 K to 300 K, Physical Review 107(4) (1957) 972.
[117] C. Schuh, J. Mason, A. Lund, Quantitative insight into dislocation nucleation from high-temperature nanoindentation experiments, Nature Materials 4(8) (2005) 617-621.
[118] R. Pei, Y. Zhao, M. Zubair, S. Yi, T. Al-Samman, Solute drag-controlled grain growth in magnesium investigated by quasi in-situ orientation mapping and level-set simulations, Journal of Magnesium and Alloys 11(7) (2023) 2312-2325.
[119] T.-W. Fan, Q. Zhang, L. Ma, P.-Y. Tang, B.-Y. Tang, L.-M. Peng, W.-J. Ding, First-principles study of the dislocation core structures on basal plane in magnesium, European Journal of Mechanics-A/Solids 45 (2014) 1-7.
[120] J. Wang, I. Beyerlein, C. Tomé, An atomic and probabilistic perspective on twin nucleation in Mg, Scripta Materialia 63(7) (2010) 741-746.
[121] N. Bertin, C. Tomé, I. Beyerlein, M. Barnett, L. Capolungo, On the strength of dislocation interactions and their effect on latent hardening in pure Magnesium, International Journal of Plasticity 62 (2014) 72-92.
[122] B. Li, Q. Zhang, S. Mathaudhu, Basal-pyramidal dislocation lock in deformed magnesium, Scripta Materialia 134 (2017) 37-41.

Contributions Arising from This Thesis

Published Journal publication:

- **Moein Imani Foumani,** Syed Taha Khursheed, Yushun Liu, Guo-zhen Zhu, Orientation-dependence of Incipient Plasticity in a Coarse-grained Mg Revealed by Nanoindentation Pop-ins, Journal of Magnesium and alloys, May. 2025

Conference presentations:

- Orientation-dependence of Dislocation-mediated Incipient Plasticity in Mg Revealed by Nanoindentation Pop-ins, Oral presentation, Microscopical Society of Canada, June, 2025
- Orientation-dependence of Incipient Plasticity in Mg-Gd Alloy By Nanoindentation technique, Oral presentation, CMSC 2024, Best presentation award
- Evaluation of Twinning Formation in a Mg-Gd Alloy Through SPM and SEM After Nanoindentation, Poster presentation, MMC 2023